J. Fluid Mech. (1991), *vol.* 225, *pp.* 445–479
Printed in Great Britain

Experimental study of turbulent swirling flow in a straight pipe

By OSAMI KITOH

Department of Mechanical Engineering, Nagoya Institute of Technology, Gokisocho, Showa-ku, Nagoya 466, Japan

(Received 24 January 1990 and in revised form 8 August 1990)

Swirling flow through a pipe is a highly complex turbulent flow and is still challenging to predict. An experimental investigation is performed to obtain systematic data about the flow and to understand its physics. A free-vortex-type swirling flow is introduced in a long straight circular pipe. The swirling component decays downstream as a result of wall friction. The velocity distributions are continuously changing as they approach fully developed parallel flow. The swirl intensity Ω, defined as a non-dimensional angular momentum flux, decays exponentially. The decay coefficients, however, are not constant as conventionally assumed, but depend on the swirl intensity. The wall shear stresses are measured by a direct method and, except in a short inlet region, are a function only of the swirl intensity and the Reynolds number. The velocity distributions and all Reynolds stress components are measured at various axial positions in the pipe. The structure of the tangential velocity profile is classified into three regions: core, annular and wall regions. The core region is characterized by a forced vortex motion and the flow is dependent upon the upstream conditions. In the annular region, the skewness of the velocity vector is noticeable and highly anisotropic so that the turbulent viscosity model does not work well here. The tangential velocity is expressed as a sum of free and forced vortex motion. In the wall region the skewness of the flow becomes weak, and the wall law modified by the Monin–Oboukhov formula is applicable. Data on the microscale and the spectrum are also presented and show quite different turbulence structures in the core and the outer regions.

1. Introduction

At present much effort has been put into developing a more comprehensive turbulence model that is applicable to complex turbulent flow. At the Stanford Conference on Complex Turbulent Flows (Klein, Cantwell & Lilley 1980–1981), the general consensus was that the models presented did not suffice for predicting practical complex flows and needed improvement. Among the many factors which make up a complex flow, streamline curvature and/or three-dimensionality are important ones in the engineering fields. Many separate studies on the effects of these factors have been made in the past. For example, Eskinazi & Yeh (1956), So (1975) and Barlow & Johnston (1988) for curved flow, and Perry & Joubert (1965), Bradshaw (1971) and Van den Berg (1982) for three-dimensional flow.

A swirling flow is a typical complex flow that is affected by streamline curvature and flow skewness in addition to adverse and favourable pressure gradients. Their combined effects on turbulence are quite unlikely to be described by a linear

combination of these factors. Thus, additional theoretical and experimental studies are needed now for such a highly complex flow.

Kobayashi & Yoda (1987) attempted to simulate numerically a swirling flow in a pipe by using a $k-\epsilon$ model and indicated that the velocity profiles obtained were quite different from experimental ones. They concluded that the eddy viscosity components were anisotropic, and that this was the main reason for the disagreement. Computations based on a Reynolds stress model were performed by Gibson & Younis (1986) for a swirling jet and by Hirai *et al.* (1987) for a swirling flow within two concentric cylinders. These investigations met with some success in predicting the flow. However, these flows were simplified versions of the swirling flow in a pipe, because in one the wall effect was excluded and in the other had no core region. Lack of systematic experimental information makes it difficult for any modeller to compare his results with real data and thereby improve the model to predict the real, physical processes in the swirling flow through a pipe.

The main objectives of this report are (*a*) to obtain systematic data including velocity distributions, wall shear stresses and full Reynolds stress components from up- to downstream sections and (*b*) to discuss the velocity law and the turbulent quantities in terms of hitherto known models in order to help explain the behaviour of the swirling pipe flow.

2. Theoretical background

For engineering purposes it is important to understand the decay process of swirl intensity along the pipe. Many workers, including Baker (1967) and Seno & Nagata (1972), have reported an exponential decay formula for the swirl on the basis of the empirical results.

For axisymmetric flow the swirl intensity Ω, the non-dimensional angular momentum flux, is defined as

$$\Omega = 2\pi\rho \int_0^{r_0} UWr^2 \,\mathrm{d}r / \rho\pi r_0^3 U_\mathrm{m}^2, \tag{1}$$

where U, W and U_m are the mean axial, tangential and bulk velocity, respectively, r and r_0 are radial position and pipe radius, and ρ is fluid density. This definition has found acceptance with many investigators.

Because the swirl intensity decays owing to the tangential wall friction, we consider it first. Integrating the tangential momentum equation written in cylindrical coordinates (r, ϕ, x), with ϕ and x the polar and axial coordinates, respectively, we obtain the tangential shear stress $\tau_{r\phi}$ as

$$\tau_{r\phi} = \rho VW + \frac{\rho}{r^2}\int_0^r r^2 \frac{\partial}{\partial x}\left(UW + \overline{uw} - \nu\frac{\partial W}{\partial x}\right)\mathrm{d}r \tag{2}$$

where V is mean radial velocity and the lower case (u, v, w) indicates fluctuating velocities. The wall tangential shear stress normalized by the $\frac{1}{2}\rho U_\mathrm{m}^2$ becomes

$$\frac{\tau_{\phi w}}{\frac{1}{2}\rho U_\mathrm{m}^2} = 2\frac{\mathrm{d}}{\mathrm{d}(x/2r_0)}\int_0^{r_0} \frac{UWr^2\,\mathrm{d}r}{r_0^3 U_\mathrm{m}^2} = \frac{1}{2}\frac{\mathrm{d}\Omega}{\mathrm{d}(x/2r_0)}. \tag{3}$$

Here $UW \gg \overline{uw}, \nu(\partial W/\partial x)$ is assumed. Downstream of the inlet region, $\tau_{\phi w}$ is expected to be a function of the swirl intensity Ω and the Reynolds number $Re\,(=U_\mathrm{m}d/\nu$, d

is a pipe diameter) but not the inlet condition. If the Reynolds number is kept constant, $\tau_{\phi w}$ can be expressed as

$$\tau_{\phi w}/\tfrac{1}{2}\rho U_{\mathrm{m}}^2 = a_1\Omega + a_2\Omega^2 + \ldots. \tag{4}$$

For extremely small Ω, only the first term is important. Substituting this relation into (3), the exponential decay formula can be obtained as

$$\Omega = \Omega_{\mathrm{r}} \exp\left\{2a_1 \frac{x - x_{\mathrm{r}}}{d}\right\}, \tag{5}$$

where Ω_{r} and x_{r} are the swirl intensity and the axial position of suitably selected reference point, respectively. This formula is the same as that assumed by others. To obtain the decay formula for large Ω, we need an accurate relation between the tangential shear stress and the swirl intensity, a formula that for the present can be obtained only by experiments.

The velocity in a pipe is the axial flow upon which the swirling components are superimposed. Thus the streamlines are spiral in the downstream direction and the turbulent structures are subject to the mixed effects of centrifugal force due to the streamline curvature and flow skewness caused by the non-uniform spiral pitch in the flow. Both of these effects on the turbulent flow have been investigated separately by many workers.

Perry & Joubert (1965) and Bradshaw (1971) pointed out that although the body of the flow is significantly skewed there exists a thin shear layer close to the wall where the flow does not skew much and obeys the ordinary law of the wall. Backshall & Landis (1969) and Kito & Kato (1984) reported that the non-skewed layer very close to the wall was observed experimentally in a swirling pipe flows. In this thin layer, denoted as a wall region hereafter, the turbulence is affected by the streamline curvature alone. Bradshaw (1969) indicated that there exists a strong similarity between the effect of buoyancy and the streamline curvature, an effect which can be estimated as the change of the mixing length, in analogy with the Monin–Oboukhov formula developed for a stratified flow. By introducing the gradient Richardson number Ri, the mixing length l can be expressed as

$$l = l_0(1 - \beta Ri) \tag{6}$$

where β is a constant and l_0 is the mixing length with no curvature effect. According to So (1975) the gradient Richardson number for the curved flow should be expressed as

$$Ri = -\frac{V_{\mathrm{t}}}{2R_{\mathrm{c}}}\left(\frac{\partial V_{\mathrm{t}}}{\partial y} - \frac{V_{\mathrm{t}}}{R_{\mathrm{c}}}\right) \Big/ \left(\frac{\partial V_{\mathrm{t}}}{\partial y} + \frac{V_{\mathrm{t}}}{R_{\mathrm{c}}}\right)^2 \tag{7}$$

where $V_{\mathrm{t}} = (U^2 + W^2)^{\frac{1}{2}}$ denotes the total velocity, y and R_{c} are distance from the wall and local radius of curvature of the streamline, respectively. In the thin wall layer an inequality, $y \ll R_{\mathrm{c}}$, is also assumed. Close to the wall a steep velocity gradient prevails and the relation $\partial V_{\mathrm{t}}/\partial y \gg V_{\mathrm{t}}/R_{\mathrm{c}}$ holds with sufficient accuracy. The mixing-length formula then reduces to

$$\left(\frac{\tau}{\rho}\right)^{\frac{1}{2}} \frac{1}{l_0} = \frac{\partial V_{\mathrm{t}}}{\partial y} + 2\beta \frac{V_{\mathrm{t}}}{R_{\mathrm{c}}}, \tag{8}$$

where τ is a total shear stress. Integrating the equation, the following velocity law can be obtained:

$$\frac{V_{\mathrm{t}}}{u_*} = \frac{1}{\kappa} \ln \frac{y u_*}{\nu} + B + \Delta V_{\mathrm{t}}^+ \tag{9}$$

where u_*, κ and B are a friction velocity based on the total wall friction, Kármán and integration constants in the conventional log law, respectively. ΔV_t^+ denotes the deviation of the velocity from the log law and is expressed as

$$\Delta V_t^+ = -\frac{2\beta}{R_c}\int_{y_0}^{y}\frac{V_t}{u_*}\mathrm{d}y + B', \tag{10}$$

where y_0 is the lower limit of the turbulent region and B' is an additional integration constant. Thus ΔV_t^+ changes linearly with $\int_{y_0}^{y} V_t/u_*\,\mathrm{d}y/R_c$ where -2β is the constant of proportionality.

Outside the wall region the skewness of the flow becomes noticeable and (6) no longer holds. Some insight into the flow skewness in this layer can be given by considering the transport equations of the Reynolds stress. In the skewed flow, the flow direction θ, shear direction θ_s and velocity gradient direction θ_g do not coincide (Van den Berg 1982). The difference between θ_s and θ_g can be estimated as follows. The transport equation for $\overline{uv}$ and $\overline{vw}$ can be written according to Launder, Reece & Rodi (1975) (referred to as the LRR model hereinafter). After boundary-layer-like approximations according to Hirai, Takagi & Matsumoto (1988), these equations become

$$\frac{\mathrm{D}}{\mathrm{D}t}(\overline{uv}) - \overline{uw}\frac{W}{r} = -\overline{v^2}\frac{\partial U}{\partial r} + \overline{uw}\frac{W}{r} - C_1\frac{\epsilon}{k}\overline{uv} + \alpha\left(\overline{v^2}\frac{\partial U}{\partial r} - \overline{uw}\frac{W}{r}\right) + \delta\left(\overline{u^2}\frac{\partial U}{\partial r} + \overline{uw}\frac{\partial W}{\partial r}\right) - \gamma k\frac{\partial U}{\partial r} + \mathrm{Diff}\,\overline{uv}, \tag{11}$$

$$\frac{\mathrm{D}}{\mathrm{D}t}(\overline{vw}) + (\overline{v^2} - \overline{w^2})\frac{W}{r} = -\left(\overline{v^2}\frac{\partial W}{\partial r} - \overline{w^2}\frac{W}{r}\right) - C_1\frac{\epsilon}{k}\overline{vw} + \alpha\left(\overline{v^2}\frac{\partial W}{\partial r} - \overline{w^2}\frac{W}{r}\right) - \delta\left(\overline{v^2}\frac{W}{r} - \overline{uw}\frac{\partial U}{\partial r} - \overline{w^2}\frac{\partial W}{\partial r}\right) - \gamma k\left(\frac{\partial W}{\partial r} - \frac{W}{r}\right) + \mathrm{Diff}\,\overline{vw}, \tag{12}$$

where k and ϵ are the kinetic energy of the turbulent motion and its dissipation rate, and the constants in (11) and (12) are $\alpha = (8+C_2')/11$, $\delta = (8C_2'-2)/11$, $\gamma = (30C_2'-2)/55$, $C_1 = 1.5$ and $C_2' = 0.4$. $\mathrm{Diff}\,\overline{u_iu_j}$ means the turbulent diffusion terms of $\overline{u_iu_j}$. According to the numerical work on a swirling flow in coaxial pipes, with the inner pipe rotating, the diffusion terms are negligibly small compared with other terms (see Hirai *et al.* 1988). For simplicity, we also assume that the material derivative terms $\mathrm{D}(\overline{u_iu_j})/\mathrm{D}t$ are small enough to be neglected. Then the shear stress direction $\theta_s = \tan^{-1}(\overline{vw}/\overline{uv})$ is approximated as

$$\tan\theta_s = \frac{\overline{vw}}{\overline{uv}} \approx \tan\theta_g + \frac{\dfrac{W}{r}(\overline{w^2}-\overline{v^2})(2-\alpha) - \delta(\overline{u^2}-\overline{w^2})\left(\dfrac{\partial W}{\partial r} - \dfrac{W}{r}\right)}{\dfrac{\partial U}{\partial r}(-\overline{v^2} + \alpha\overline{v^2} + \delta\overline{u^2} - \gamma k)}, \tag{13}$$

where

$$\theta_g = \tan^{-1}\left[r\frac{\partial}{\partial r}\left(\frac{W}{r}\right)\Big/\frac{\partial U}{\partial r}\right].$$

Terms that include $\overline{uw}$ are neglected because of their smallness compared with other normal stress components, see results from §6. Unlike the eddy viscosity model, which predicts that the shear stress and velocity gradient are in the same direction, this relation shows that θ_s and θ_g are in general different. Depending on the second

term on the right-hand side, especially on the sign of $\partial U/\partial r$ and/or $\overline{w^2}-\overline{v^2}$, a complex angle relation is expected.

The measured Reynolds normal stresses are convenient to use to check the quality of the turbulence models. One of the most important but difficult points is the modelling of a pressure–strain term which consists of the return-to-isotropy and the rapid parts. Each includes an empirical constant, C_1 or C_2, that should be determined from appropriate experimental results. Adopting the LRR simplified model for the rapid part, and applying similar approximations to the transport equations for $\overline{u^2}$ and $\overline{v^2}+\overline{w^2}$ as before, we obtain

$$0 = -2\overline{uv}\frac{\partial U}{\partial r} - C_1\frac{\epsilon}{k}(\overline{u^2}-\tfrac{2}{3}k) + 2C_2\,\overline{uv}\frac{\partial U}{\partial r} + \tfrac{2}{3}C_2P' - \tfrac{2}{3}\epsilon, \tag{14}$$

$$0 = -2\overline{vw}\left(\frac{\partial W}{\partial r}-\frac{W}{r}\right) - C_1\frac{\epsilon}{k}(\overline{v^2}+\overline{w^2}-\tfrac{4}{3}k) + 2C_2\,\overline{vw}\left(\frac{\partial W}{\partial r}-\frac{W}{r}\right) + \tfrac{4}{3}C_2P' - \tfrac{4}{3}\epsilon, \tag{15}$$

where

$$P' = -\overline{uv}\frac{\partial U}{\partial r} - \overline{vw}\left(\frac{\partial W}{\partial r}-\frac{W}{r}\right).$$

At the radial positions where the mean strain rate vanishes,

$$\partial U/\partial r = 0 \quad \text{or} \quad \partial W/\partial r - W/r = 0,$$

equations (14) and (15) reduce to a set of simple algebraic relations for the normal stresses

$$\left.\begin{aligned} &\text{at}\quad \frac{\partial U}{\partial r}=0;\quad \frac{\overline{u^2}}{k}=\frac{2}{3}+\frac{2}{3C_1}(C_2-1),\\ &\text{at}\quad \frac{\partial W}{\partial r}-\frac{W}{r}=0;\quad \frac{\overline{v^2}+\overline{w^2}}{k}=\frac{4}{3}+\frac{4}{3C_1}(C_2-1). \end{aligned}\right\} \tag{16}$$

Adopting an elaborate version for the rapid part in the LRR model, the $\overline{u^2}/k$ relation becomes

$$\text{at}\quad \frac{\partial U}{\partial r}=0;\quad \frac{\overline{u^2}}{k}=\frac{2}{3}+\frac{2}{3C_1}(\alpha+\beta-1). \tag{17}$$

It is now easy to compare the above relations with the experimental data.

3. Experimental equipment and methods

Two different types of facilities have been used for measuring different variables. One is a system using air as working fluid to measure the velocity and the Reynolds stress distributions by means of a hot-wire anemometer. The other adopts water as the working fluid in order to measure the wall shear stress and the decay of angular and axial momentum fluxes along the pipe.

Figure 1 shows the general arrangement of the equipment for the air flow experiment. The test pipe is 150 mm in internal diameter d and 7000 mm long, having a hydraulically smooth surface. At the upstream end of the pipe there is a settling chamber in which a swirling generator is installed. A blower driven by a variable-speed motor and a venturi meter for measuring flow rate are connected at the downstream end. The axial position x is defined as the distance from the inlet section of the pipe. The swirling component is generated by 24 guide vanes in the

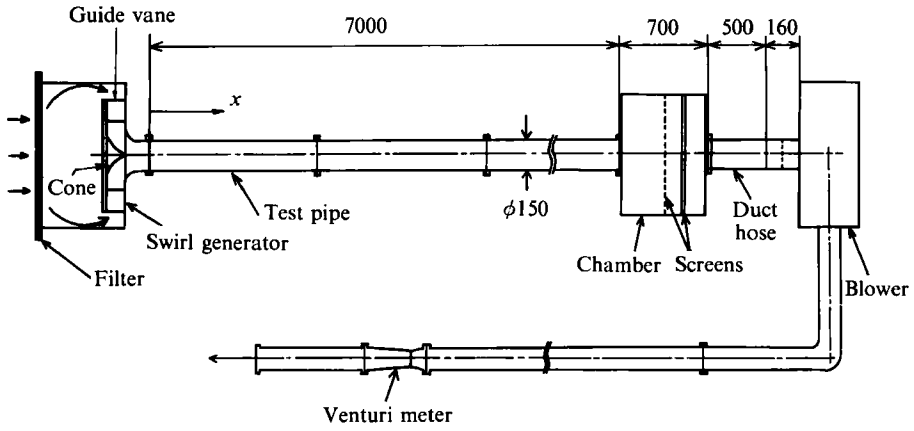

FIGURE 1. Experimental apparatus. Dimensions in mm.

Test section (TS)	1	2	3	4	5	6	7	8	9	10	11
x/d	5.7	7.7	12.3	14.3	19.0	21.0	25.7	28.0	32.4	39.0	43.3
Run 1, $Re = 6\times10^4$	—	1.42	—	1.18	—	0.89	—	0.68	0.64	0.57	—
Run 2, $Re = 6\times10^4$	—	0.71	—	0.58	—	0.53	—	—	0.35	0.36	0.30
Run 3, $Re = 6\times10^4$	—	0.28	—	0.24	—	0.21	—	—	0.12	0.15	0.14
Run 4, $Re = 6\times10^4$	—	—	—	—	—	—	—	—	—	—	0.11
Run 5, $Re = 4\times10^4$	—	—	—	—	—	—	—	—	—	—	0.07
Run 6, $Re = 8\times10^4$	—	—	—	—	—	—	—	—	0.16	—	—
Run 7, $Re = 5\times10^4$	—	—	1.18	—	—	—	0.79	—	—	0.57	—
Run 8, $Re = 5\times10^4$	0.97	—	0.83	—	0.67	—	0.60	—	0.47	0.42	—
Run 9, $Re = 5\times10^4$	—	—	0.59	—	—	—	0.43	—	—	0.36	—
Run 10, $Re = 5\times10^4$	—	—	0.24	—	—	—	0.18	—	—	0.12	—

TABLE 1. Velocity measuring sections and swirl intensities. The numbers indicate swirl intensity Ω.

generator along which the flow passes radially inward. The vane angle can be fixed by pins at 10° intervals from zero to 60° with respect to the radial direction. Six different swirl intensities can be obtained. The bell-shaped cone at the centre of the swirler smoothly deflects the radial flow in the axial direction (Yajnik & Subbaiah 1973). The flow rate can be adjusted by controlling the variable-speed motor. The experimental Reynolds numbers Re based on the average bulk velocity U_m and pipe diameter d are 40000, 50000, 60000 and 80000.

The measuring sections are prepared at the axial positions along the pipe shown in table 1, at each of which there is a probe inserting hole. The measuring sections (test sections) are denoted by TS in the figures and tables. Various types of hot-wire probes are traversed radially through the hole to measure the mean velocities and the Reynolds stresses. For measuring the flow angle θ and the time mean velocity, an I-type hot wire made of tungsten (5 μm in diameter) having a sensing length of 1 mm is used. Both end regions of the wire are copper plated (25 μm in diameter). As shown later, the radial velocity is extremely small compared with the other components, so the velocity vector is almost parallel to the wall. Using the flow angle θ and the resultant velocity V_t, the axial and tangential velocity components U and W can be easily obtained. Figure 2 shows the velocity components and the coordinate system used.

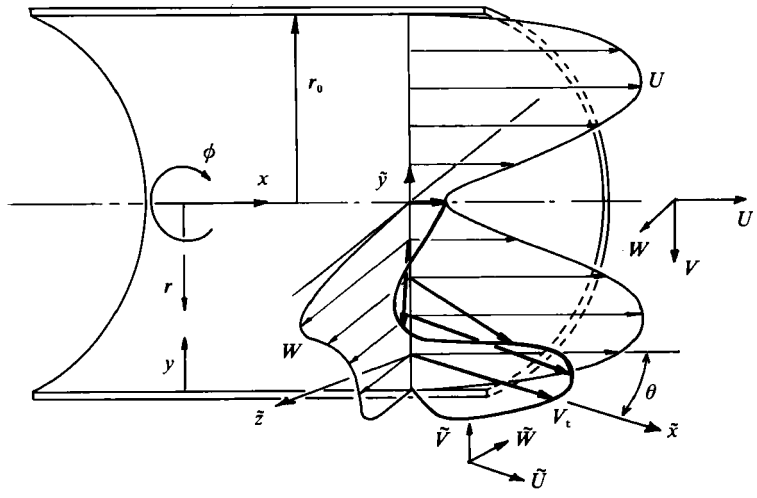

FIGURE 2. Coordinate systems and velocities.

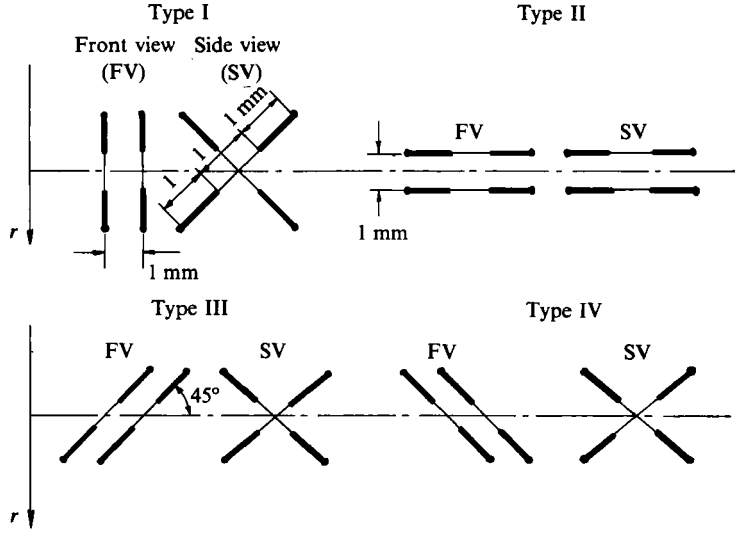

FIGURE 3. Types of ×-wires used.

The complete set of Reynolds stress components are measured using the four different types of ×-wires shown in figure 3. They are similar in shape but have different orientations, i.e. every 45°, along the probe axis. The measuring principle for the $\overline{u_i u_j}$ is based on that of Müller (1982*b*). Fourteen sets of r.m.s. data of the fluctuating velocity obtained per measurement point from these probes, aimed in the local flow direction, are enough to obtain all $\overline{\tilde{u}_i \tilde{u}_j}$ components. The tilde indicates variables that are evaluated in the local coordinate system $\tilde{x}$, $\tilde{y}$ and $\tilde{z}$, where $\tilde{x}$ is directed to the flow direction and $\tilde{y}$ normal to the wall. The transformation from the local to the laboratory system (r, ϕ, x) can be made by simple algebra.

The nonlinear response of the hot wire to the oncoming velocity causes some error in estimating the turbulent intensity. Müller (1982*b*) indicated that neglecting moments of the fluctuating velocity larger than the second induces some error when

×-wire type	$\overline{\tilde{u}^2}$	$\overline{\tilde{v}^2}$	$\overline{\tilde{w}^2}$	$\overline{\tilde{u}\tilde{v}}$	$\overline{\tilde{u}\tilde{w}}$	$\overline{\tilde{v}\tilde{w}}$
I	○	○		○		
II	○		○		○	
III						○
-------	○*			○*	○*	
IV						○

TABLE 2. ×-type hot wires and Reynolds stresses that can be measured. (*: Combination use of two probes.)

the turbulent intensity exceeds 20%. Also, since the sensor has a finite size, another error becomes appreciable when it is used in a region of steep velocity gradient, i.e. in the central region and regions close to the wall in a swirling flow. To estimate the accuracy of the measured Reynolds stresses, the redundant data from different sets of measurements and another measuring method are compared. Table 2 shows the components of $\overline{\tilde{u}_i \tilde{u}_j}$ that can be measured by these probes. Figure 4 compares the measured data from different ×-wire types, and it includes results from rotating a single wire (a method based on that of Bissonette & Mellor 1974). Consistency among the data is very good except in the regions close to the wall and the pipe axis. Arrows in the figure indicate the region of high turbulent intensity, larger than 20 or 10%. Thus we conclude that the measured Reynolds stress data are reliable within $\pm 0.001 U_m^2$ except in the region of high turbulent intensity (>10%) and steep velocity gradient. Hereafter the high-turbulence region (>10%) is denoted by broken lines.

For measuring the wall shear stress and the momentum fluxes, a test pipe of 50.8 mm inner diameter and 4000 mm long is used with the same type of swirl generator but of reduced size placed at the upstream end. A three-hole cylindrical Pitot tube, 2.5 mm in outer diameter, is used to measure the velocity components U and W for evaluation of the non-dimensional angular momentum flux Ω, the swirl intensity. In a swirling flow the wall shear stress is difficult to measure by the indirect method, which is based on the existence of the universal wall law. The wall law is modified by the centrifugal force due to the rotating motion of the fluid, and one cannot expect it to be a sound basis for indirect methods.

Here a shear-stress meter based on the direct method is developed. Figure 5 shows the structure of the meter for the tangential wall shear stress $\tau_{\phi w}$. The sensing element that is separated from the pipe system is suspended by two plate springs so that it can be rotated by a small amount around the pipe axis if a torque is applied to the element. The torque can be evaluated by measuring the rotation angle because a linear relation exists between them for a limited torque range. The rotation angle can be measured by the change of the distance between the target plate fixed on the element and the electric eddy current probe. There are many error sources for a direct shear stress meter as described by Allen (1977), and these sources are carefully removed in our meter. The stiffness coefficient of the spring is selected so that the torque resolution becomes as small as 8×10^{-7} N m. The wall shear stress measured by this meter is the average over the element surface, which is 24 mm in length ($0.47d$). The evaluated mean value does not coincide exactly with the local wall shear stress, because in general the swirling flow is axi-asymmetrical (Kito 1984), and the shear stress is distributed around the periphery of the pipe. To check the final accuracy of this meter, the well-defined laminar flow between two concentric

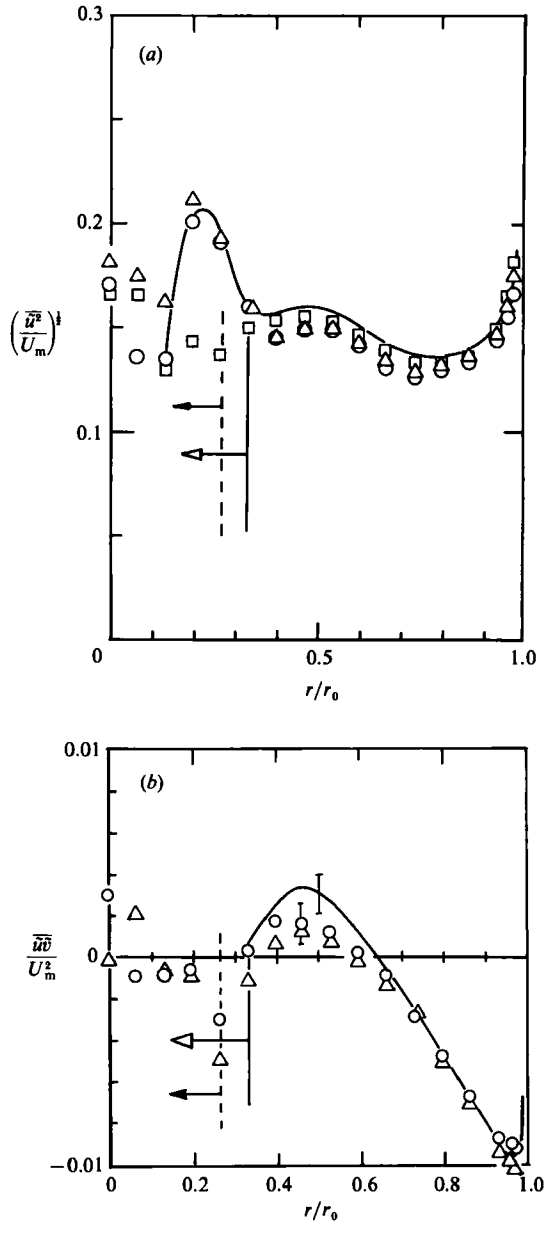

FIGURE 4. Accuracy of Reynolds stresses measured by ×-wires. ×-wire type: △, I; □, II; ○, III, IV. ——, Single rotating wire (Bissonette & Mellor 1974). Regions of turbulent intensity larger than 20% (——▶) and 10% (——▷). Error bars indicate an uncertainty band of $\pm 0.001 U_m^2$.

cylinders, the inner one rotating, is used. The measured torque coefficients coincide with the theoretical ones to within an accuracy of ±3.5% of the reading (20:1 odds). For measuring the axial wall shear stress τ_{xw}, the same meter is used, except that eight music wires are used instead of the spring. The force resolution is 1.5×10^{-4} N. The accuracy of the data is checked by measuring τ_{xw} in fully developed pipe flow and comparing with the Blasius or Nikradse formulae. The accuracy is estimated to be ±4% of the reading (20:1 odds).

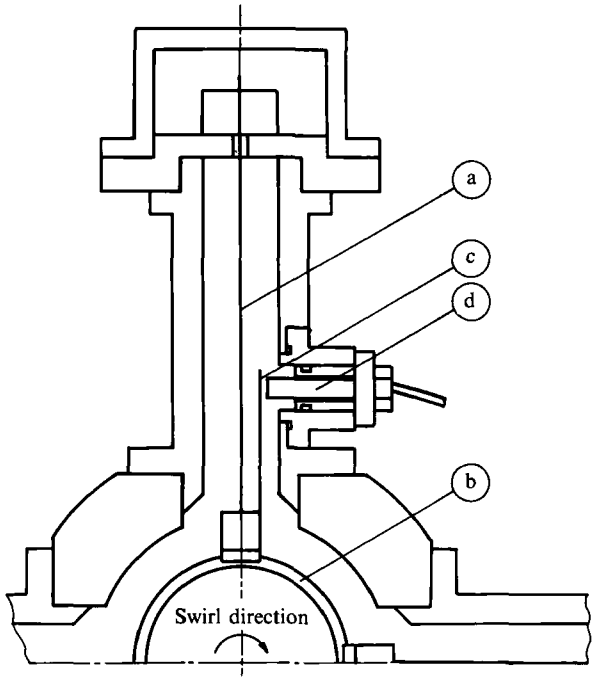

FIGURE 5. Wall-shear-stress meter: a, plate spring; b, sensing element of pipe; c, target plate; d, electric eddy current probe.

4. Decay of swirl intensity and wall shear stress

The definition of the swirl intensity Ω, a non-dimensional angular momentum flux, is different from that used by Yajinik & Subbaiah (1973) and Seno & Nagata (1972), for example. They defined it as the ratio of angular to axial momentum flux. The numerical values, however, do not differ very much. A downstream change of the swirl intensity in either definition shows an exponential decay along the pipe axis as in equation (5). Seno & Nagata (1972) considered the effect of the pipe roughness and Baker (1967) and Padmanabhan & Janek (1980) studied the effect of the Reynolds number and inlet swirl intensity on the decay.

Figure 6 shows the decay of Ω plotted on a semi-log map at $Re = 50000$ for various inlet swirl intensities, Ω being evaluated from the Pitot tube measurements. The abscissa x' is defined as the distance from the virtual origin x_0. The x_0 are selected so that each decay curve for a different inlet swirl intensity would fall along a single curve. The decay curve is approximately linear but has a 'knee' point at $\Omega = 0.1$. Thus the decay coefficient $2a_1$ in (5) is expected to depend on the swirl intensity. A more detailed picture of the decay coefficient can be obtained from the relation between the tangential wall shear stress $\tau_{\phi w}$ and Ω. Figure 7 shows this relation, the former measured by the shear-stress meter, for various inlet swirl intensities. To obtain the data the shear-stress meter was successively moved from $x/d = 6.3$ to 80.3 in increments of $5d$. The data fall along a single curve, denoted by the solid line in the figure, irrespective of the different inlet swirl intensities except in the inlet region, the portions denoted by broken lines. The arrows on the line show the downstream direction. Thus $\tau_{\phi w}$ can be expressed as a function of Ω except in the inlet region. The solid line has clear deflection points at $\Omega = 0.09$, 0.45 and a less clear one at $\Omega = 0.04$.

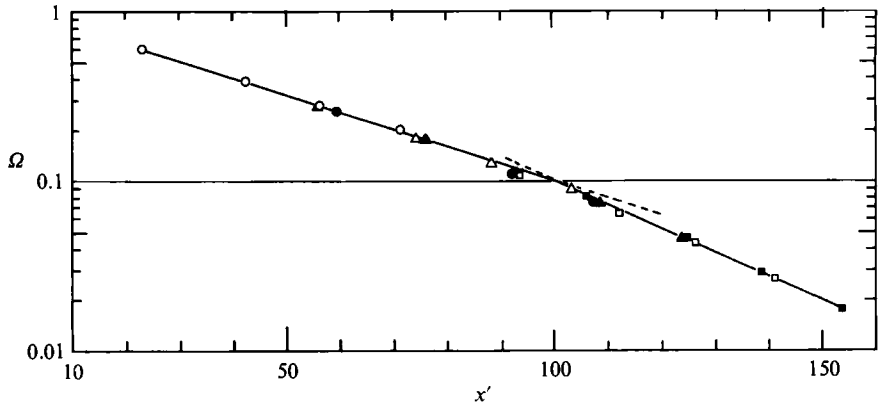

FIGURE 6. Decay of swirl intensity Ω along pipe axis at $Re = 50000$, x' is distance from the virtual origin x_0. Swirl intensity and distance at initial reference section ($x/d = 23.4$); ○, $\Omega = 0.6$, $x_0/d = 0$; △, $\Omega = 0.277$, $x_0/d = 32$; ●, $\Omega = 0.256$, $x_0/d = 36.1$; ▲, $\Omega = 0.173$, $x_0/d = 52.6$; □, $\Omega = 0.102$, $x_0/d = 70.2$; ■, $\Omega = 0.081$, $x_0/d = 82.6$.

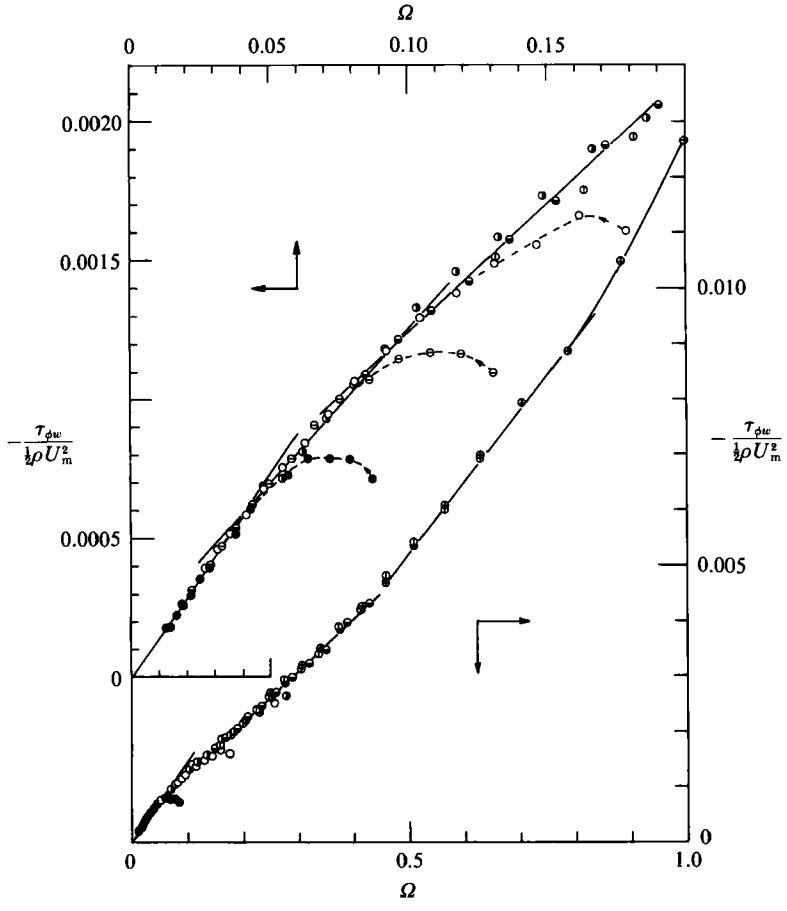

FIGURE 7. Relation between tangential wall shear stress and Ω. Initial swirl intensity estimated at $x/d = 6.3$: ⊕, $\Omega = 0.966$; ⊕, 0.631; ◒, 0.431; ◑, 0.279; ○, 0.178; ⊖, 0.130; ●, 0.086.

	$Re = 50000$		$Re = 100000$		$Re = 150000$	
Ω	$2A_i$	B_i	$2A_i$	B_i	$2A_i$	B_i
0–0.04	−0.038	0	−0.0291	0	−0.0282	0
0.04–0.09	−0.0274	−0.000131	−0.0227	−0.000128	−0.0206	−0.00013
0.09–0.45	−0.0208	−0.000425	−0.0187	−0.000313	−0.0152	−0.000406
0.45–0.80	−0.0277	0.000987	−0.0257	0.0119	−0.0253	0.0016

TABLE 3. The coefficients $2A_i$ and B_i in the relation between $\tau_{\phi w}$ and Ω.

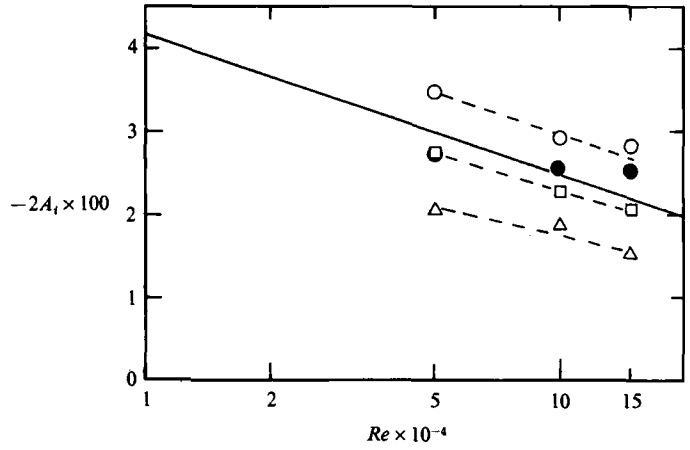

FIGURE 8. Decay coefficient of Ω: ○, $-2A_1$; □, $-2A_2$; △, $-2A_3$; ●, $-2A_4$; ——, Baker's (1967) result.

The change of the slope at $\Omega = 0.09$ corresponds to the knee point in figure 7, but those at 0.45 and 0.04 have no clear corresponding points on the swirl decay curve. If we assume piecewise linear relations between the knee points, $\tau_{\phi w}$ can be expressed as

$$\tau_{\phi w}/\tfrac{1}{2}\rho U_{\mathrm{m}}^2 = A_i \Omega + B_i, \quad i = 1, \ldots, 4.$$

The constants A_i and B_i are tabulated in table 3. Using the linear relation of $\tau_{\phi w}$ with Ω, the decay formula can be expressed as

$$\log\left(\Omega + \frac{B_i}{A_i}\right) = 2A_i \frac{x - x_{\mathrm{r}}}{d} + \log\left(\Omega_{\mathrm{r}} + \frac{B_i}{A_i}\right).$$

The exponential decay law is correct only in the range $0 < \Omega < 0.04$, because $B_1 = 0$ here. When $B_i \ll A_i$, the exponential decay law holds approximately and $2A_i$ is nearly equal to a decay coefficient, $2a_1$. Figure 8 compares the coefficients $2A_i$ to the decay coefficient reproduced from Baker's (1967) diagram. Basically, it decreases with Re. The difference of $2A_i$ for various ranges of Ω is significant; in the range $0.09 < \Omega < 0.45$, $2A_i$ is especially small compared with those for different Ω.

The variations of the axial wall shear stress τ_{xw} with Ω for three Re values are shown in figure 9. τ_{xw} increases noticeably with Ω, and is almost double the zero-swirl value at $\Omega = 0.55$. The Reynolds-number dependence of the wall shear stresses can be estimated by considering the variation of a friction factor of the pipe, λ, with Re like

$$\frac{\tau_{xw}(Re_1)}{\tau_{xw}(Re_2)} = \frac{\lambda(Re_1)}{\lambda(Re_2)}, \tag{18}$$

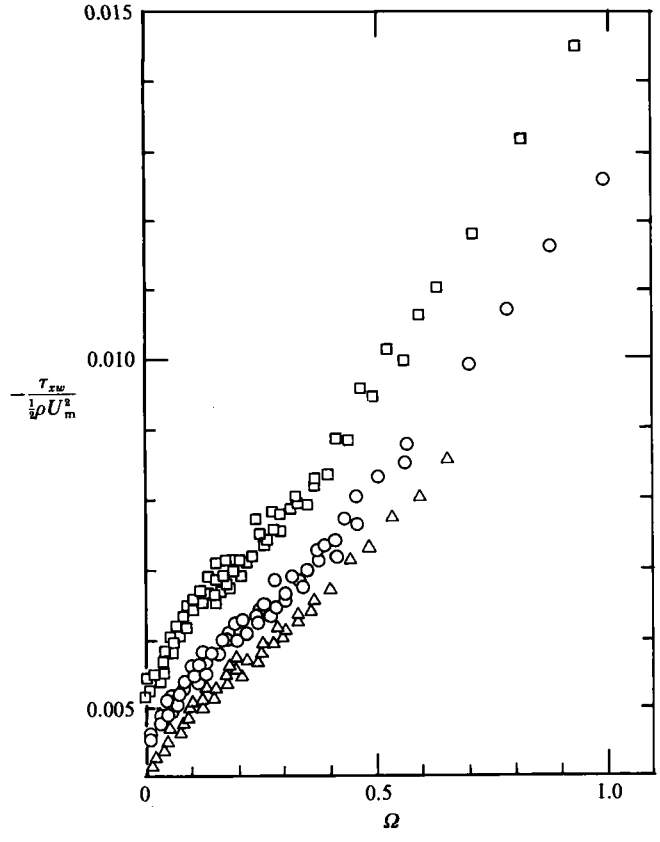

FIGURE 9. Relation between axial wall shear stress and Ω: □, $Re = 50000$; ○, $Re = 100000$; △, $Re = 150000$.

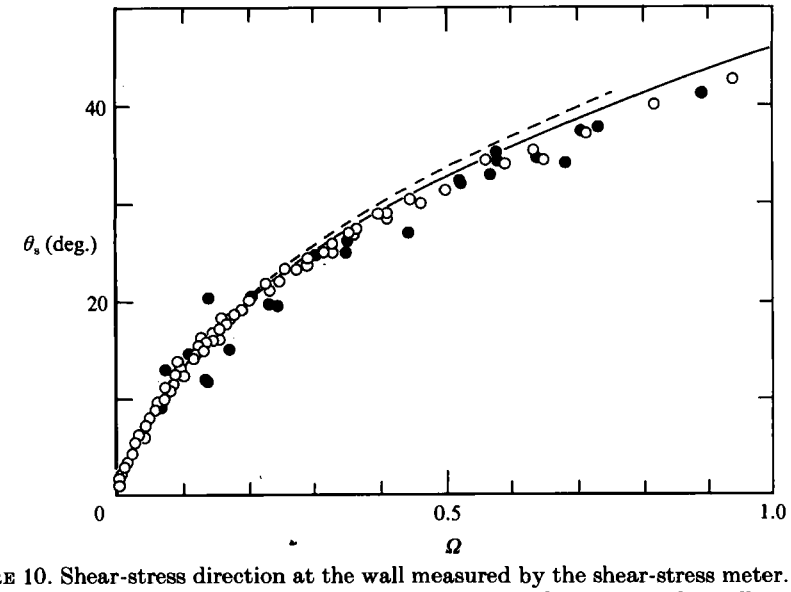

FIGURE 10. Shear-stress direction at the wall measured by the shear-stress meter. ○, $Re = 50000$; ——, $Re = 100000$; – – – –, $Re = 150000$; ●, streamline direction at the wall measured by a hot-wire anemometer.

which is within an accuracy of $\pm 2\%$ in the range of $5\times10^4 < Re < 15\times10^4$. A similar relation holds for tangential shear stress to within $\pm 5\%$ accuracy. The shear-stress direction θ_s at the wall changes with Ω and the relations measured by the shear-stress meter are shown in figure 10. The limiting streamline angles with respect to the pipe axis measured by a hot-wire anemometer are also included in the figure. The overall agreement between the two methods is good. Some scatter of the data from the hot wire is seen at around $\Omega = 0.2$. Kito (1984) reported that axisymmetry of the velocity profile fails near $\Omega = 0.2$, so that the local streamline direction at the wall also becomes asymmetrical with respect to the pipe axis, and this appears to be the main reason for the scatter of the data from a hot wire.

The wall shear stress data $\tau_{\phi w}$ and τ_{xw} presented here are average values over the pipe circumference and would be appropriate for comparing with the results of a numerical simulation of swirling flow, for in numerical work it is usually assumed that the time-mean values are axisymmetrical.

5. Velocity distributions

Figure 11 (*a*, *b*) shows the profiles of tangential and axial velocity distributions W, U at various stations along the pipe axis as measured by a hot-wire anemometer. From the shape of the tangential velocities the swirling flow has a three-region structure consisting of wall, annular and core regions. In the wall region the velocity gradient is quite steep and, as described later, the flow skewness here is negligibly small. The annular and core regions are characterized by free- and forced-vortex-type velocity distributions, respectively. In the figure the distribution of a pure forced–free vortex model (Rankin's combined vortex) is shown for comparison. Except in the region around the meeting point of two vortices, the Rankin vortex is a reasonable qualitative model of the tangential velocity distribution unless Ω is too low. The extent of each vortex region changes in accordance with the swirl intensity. In a weak swirl, Ω less than 0.2, the boundary between the core and annular regions becomes obscure, and finally, when $\Omega \leqslant 0.1$, the forced-vortex-type motion dominates the whole section.

Pressure within the section can be estimated from

$$P = P_w - \rho \int_r^{r_0} \left\{ \frac{W^2}{r} - \frac{1}{r}\frac{\partial}{\partial r}(r\overline{v^2}) \right\} \mathrm{d}r$$

where $\overline{w^2} \ll W^2$ is assumed. Using the turbulence data to be given later, the effect of normal stress on the pressure distribution is less than 3%. The wall pressure P_w is measured as a mean value from four pressure holes that are equally spaced around the circumference. Figure 12 shows the pressure distributions across the section. Owing to the swirl decay along the pipe axis, the centrifugal force weakens and adverse and favourable pressure gradients appear in the centre and outer regions, respectively. These pressure gradients have a considerable effect on the axial velocity distributions, i.e. a low velocity in the centre region surrounded by high velocity in the annular region, figure 11 (*b*). When the swirl intensity is larger than 0.4, in our experiment, the reverse flow appears at the centre and its magnitude and the area increase as Ω increases.

The radial velocity V is estimated from a continuity equation

$$V = -\frac{1}{r}\int_0^r \frac{\partial}{\partial x}(rU)\,\mathrm{d}r$$

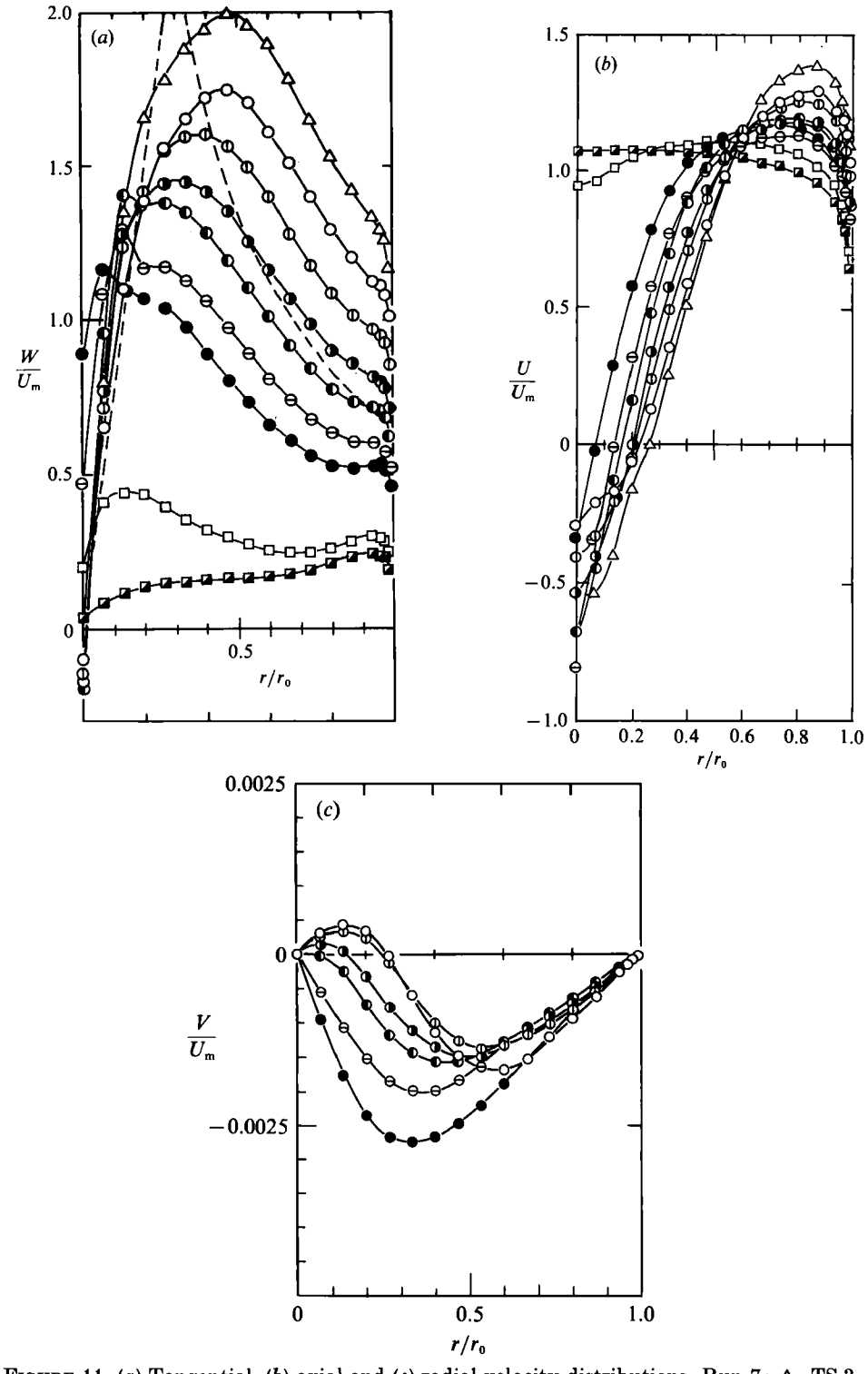

FIGURE 11. (*a*) Tangential, (*b*) axial and (*c*) radial velocity distributions. Run 7: △, TS 3. Run 8: ○, TS 1; ⊕, TS 3; ◑, TS 5; ◐, TS 7; ⊖, TS 9; ●, TS 10. Run 10: □, TS 7; ◪, TS 10. ----, Rankin combined vortex. (TS and runs shown in table 1.)

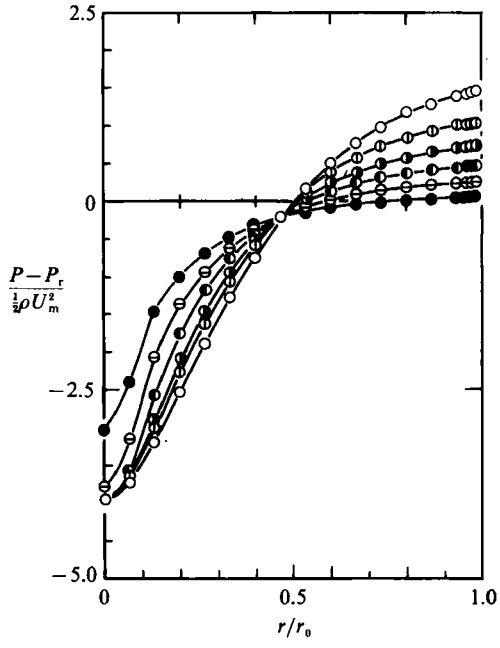

FIGURE 12. Pressure distribution across a section. P_r is a reference pressure ($=P_w(x/d = 41.1)$). For symbols, see figure 11.

and the distributions of V in a cross-section are shown in figure 11 (c). The magnitude of V is of order 1/1000 of the average axial velocity U_m, and the total velocity direction is considered to be almost parallel to the wall surface.

5.1. *Wall region*

Figure 13 examines the skewness of the flow close to the wall by plotting U versus W. Up to some point from the wall the flow angle does not change, collateral flow, and it then changes gradually as the wall distance increases. For a three-dimensional flow developed on a flat plate, Johnston (1970) and Perry & Joubert (1965) reported that the edge of the constant-flow-angle region is at 60–100, or 150 in the wall variable y^+. Here this edge point is situated at around 60. The centrifugal force is the dominant term that affects the flow within this constant-angle region. Figure 14 (a–c) shows semi-log plots of V_t for (a) weak, (b) moderate and (c) strong swirl intensity and in comparison with the conventional log law. The friction velocity is estimated from the velocity gradient at the wall. In the range $0 < \Omega < 0.11$ the velocities follow the conventional log law up to $y^+ \approx 200$ and the streamline curvature has no effect on the flow. For swirl intensity larger than $\Omega > 0.3$, the data ($y^+ < 1000$) fall along a single curve with a smaller slope than the conventional curve, irrespective of the swirl intensity. This means that the centrifugal force effect on the turbulence is saturated when Ω exceeds 0.3. In the intermediate swirl intensity range, the slope changes gradually with Ω. Thus, within the rather narrow range of Ω from 0.1 to 0.3, the centrifugal force effect on the turbulence starts and reaches saturation.

The deviation of the velocity from the log law ΔV_t^+ can be expressed by equation (10). The excess value of the velocity ΔV_t^+ is plotted in figure 15 against $1/R_c \int_0^y (V_t/u_*)\,dy$. Here the lower limit of the integration is zero instead of y_0, which results in only a small change in the abscissa. In the range $0.02 < 1/R_c \int_0^y (V_t/u_*)\,dy < 0.1$ the

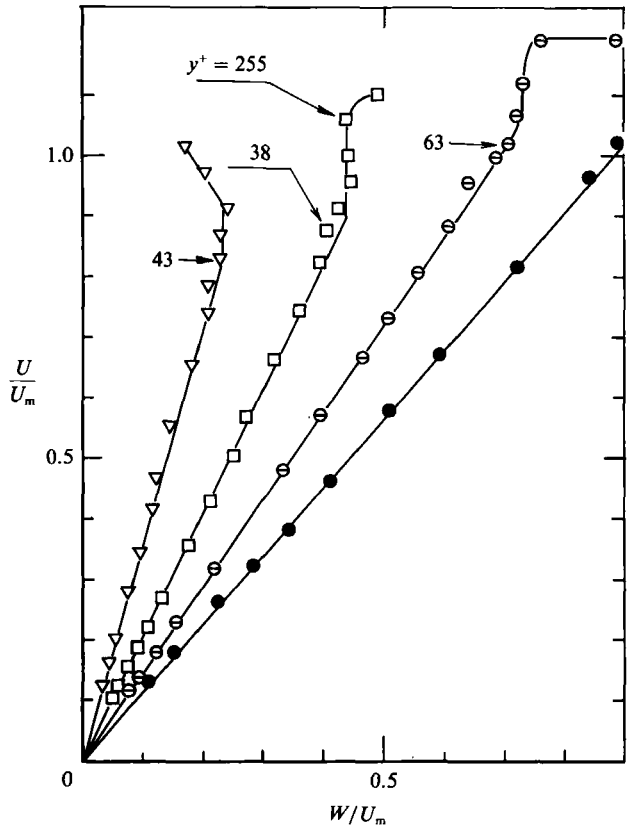

FIGURE 13. Flow skewness in the near-wall region. Run 1: ●, TS 6; ⊖, TS 9. Run 2: □, TS 9. Run 3: ▽, TS 9.

data for ΔV_t^+ fall on a line of slope -12. The furthest extent of the validity of (10), i.e. the wall region, is thus considered to be the y-coordinate that gives an integral value of 0.1. According to (10), this result shows that the constant $\beta = 6$. The constant in the Monin–Oboukhov formula has been reported by many workers for a flow passing through a curved or rotating channel and it is distributed in the range $2 < \beta < 7$ for small Richardson number. An overall review for β was given by So (1975) and he recommended $\beta = 2.5$ from among the many previously proposed values. The result obtained here is not consistent with So but it is the same as that obtained by Johnston, Halleen & Lezius (1972) for rotating channel flow.

The slope of the log formula in the semi-log diagram, equal to the inverse of the Kármán constant $1/\kappa$, changes as the streamline curvature effect appears. Here the change of κ with Ω can be used as a measure of the curvature effect on the flow in the wall region (figure 16). From $\Omega = 0.1$ to around 0.3–0.4 it increases from the known value of 0.41 to the final value of 0.725.

The change of the Richardson number with Ω is interesting, for it also expresses quantitatively the curvature effect. The figure also shows the change of $-Ri$ estimated at $y^+ = 100$ with Ω. The magnitude of Ri increases from 0.05 at $\Omega = 0.1$ to a final value of 0.27 at $\Omega = 0.4$–0.5. The curve is very similar with that of κ. The curvature effect is almost saturated at around $\Omega = 0.4$–0.5. Although there exists some scatter in the data points, $-Ri$ at $\Omega = 0.1$ is about 0.05. Townsend (1976)

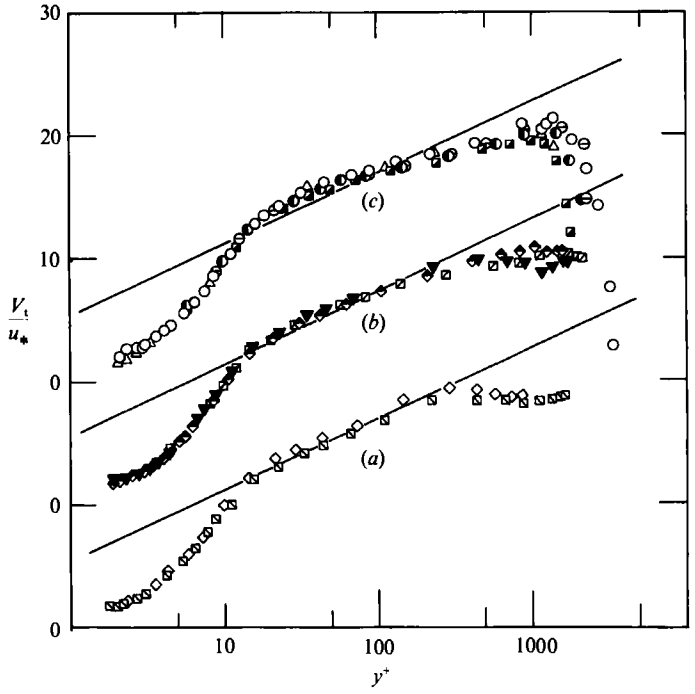

FIGURE 14. Log law in swirling flow, (*a*) weak swirl, (*b*) moderate swirl, (*c*) strong swirl. ——, $V_t/u_* = 2.5 \ln y^+ + 5.5$. Run 1: ○, TS 2; ●, TS 6; ⊖, TS 9; ◐, TS 10. Run 2: ◓, TS 4; ◒, TS 6; □, TS 9; ■, TS 10; ◪, TS 11. Run 3: ▲, TS 6; ▼, TS 10; ◪, TS 11. Run 4: ◪, TS 11. Run 5: ◇, TS 11. Run 6: ◆, TS 9.

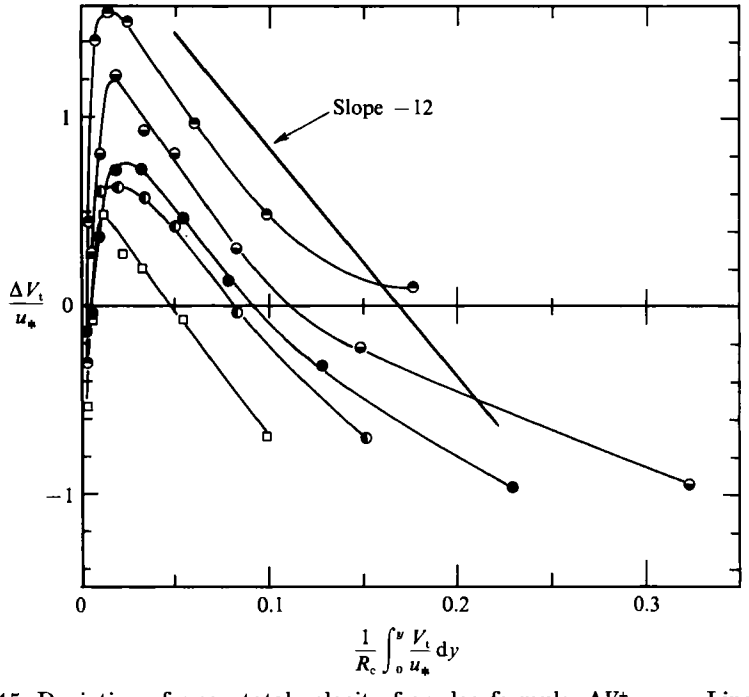

FIGURE 15. Deviation of mean total velocity from log formula, ΔV_t^+. ——, Line of slope −12. For symbols, see figure 14.

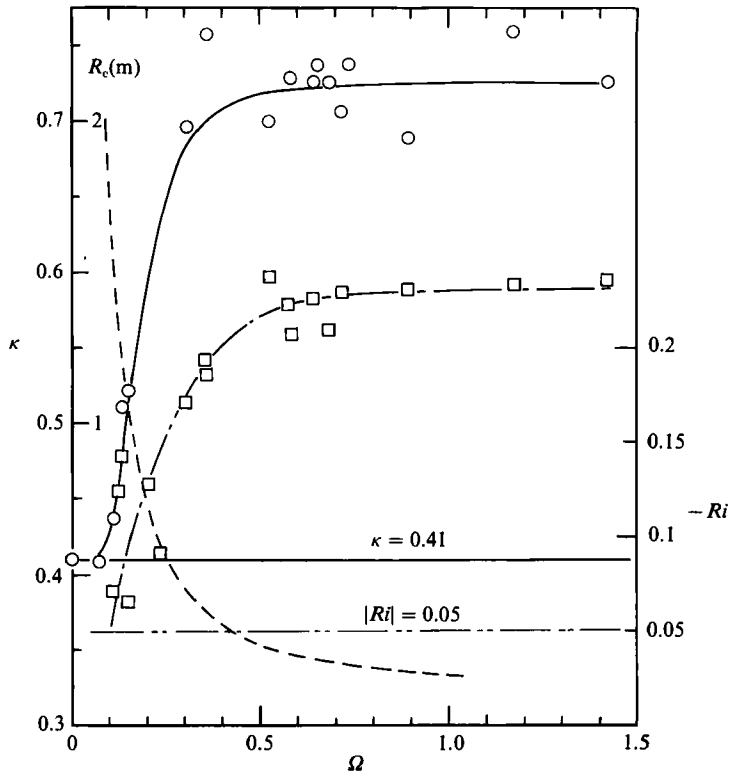

FIGURE 16. Effects of swirl intensity Ω on the Kármán constant κ, Richardson number Ri and radius of streamline curvature R_c: —○—, κ; —·—□—·—, Ri at $y^+ = 100$; ----, R_c; ——·——·——, above this Ri line, the effect of centrifugal force on the flow becomes appreciable, Townsend (1976).

suggested that the curvature effect becomes appreciable when $|Ri| \geqslant 0.05$. This suggestion is consistent with the present result that the centrifugal force becomes important if Ω exceeds 0.1. Such a rapid change of κ or Ri from $\Omega = 0.1$ to 0.5 and its almost levelling off beyond 0.5 can be explained by the change of radius of streamline curvature with Ω. The radius of streamline curvature R_c at the wall can be estimated as $\frac{1}{2}d/(\sin^2\theta)$. Using the data for θ in figure 10, the R_c curve in figure 16 was estimated. From $\Omega = 0.1$ to 0.3, R_c decreases rapidly as Ω increases, but its reduction rate becomes smaller. Beyond $\Omega = 0.5$, R_c does not change so much and the curvature effect is almost saturated there.

5.2. *Annular region*

Figure 17 shows the distributions of θ, θ_g and θ_s (i.e. flow, velocity gradient and shear stress angles, respectively). The hatched region in the figure indicates the wall region and the three angles coincide there. Beyond the wall region in the annular region, different angle relations become noticeable: θ_s and θ_g change rapidly along r, whereas changes in θ are slower. Thus, in this region the flow and shear directions skew and the three angles do not coincide with each other. The turbulent motion contains the skewness effect in addition to the curvature effect. We cannot expect the simple mixing-length model of turbulence to work well here.

In this region the tangential velocity approximates a free-vortex-type distribution.

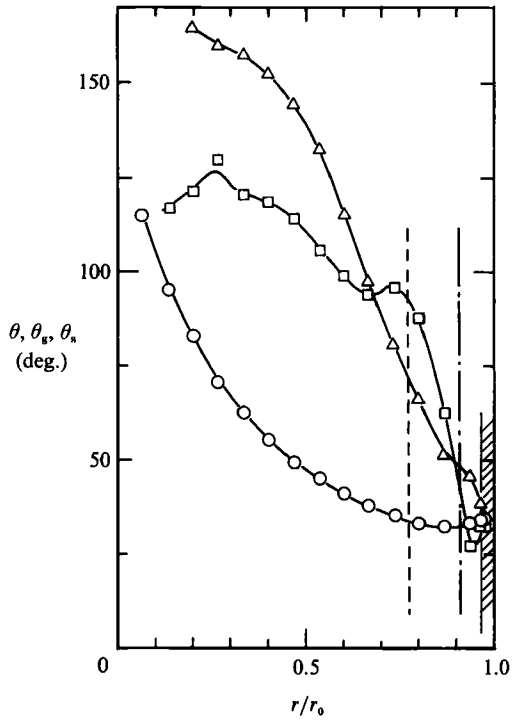

FIGURE 17. Relations among angles θ, θ_g and θ_s. Run 8, TS 7: ○, θ; □, θ_g; △, θ_s; ----, radial position of $\partial U/\partial r = 0$; —·—·—, radial position of $\overline{w^2} - \overline{v^2} = 0$. Shaded region is the wall region.

As the swirl decays downstream, the velocity distribution changes from a free vortex to a forced vortex type. For a nearly plane swirling flow (the axial gradient is very small compared to the radial gradient) Reynolds (1961) indicated that a free-vortex-type flow is expected from an order estimation of the momentum equation. This estimation was substantiated by the work of Hirai *et al.* (1987) who measured the free vortex motion in a plane swirling flow within two concentric cylinders, the inner one rotating and the axial velocity component being superimposed on it. In the swirling flow decaying downstream, however, the effect of axial transport of momentum becomes important as shown later and the momentum balance among many terms becomes more complicated than in the plane swirling flow case. In this case we cannot say anything about the velocity distributions from a theoretical standpoint. From a phenomenological point of view, we assume that the tangential velocity in the decaying swirling flow can be expressed as a modification of the plane swirling flow like

$$\frac{W}{U_m} = \frac{C}{r/r_0} + f\left(\frac{r}{r_0}\right), \tag{19}$$

where $f(r)$ is some modification function of r to be added to the free vortex. After trying various forms of $f(r)$ and considering that the final state of the tangential velocity is a forced vortex, $f(r)$ should be a linear function of r: $f(r) = \omega r/r_0$. Equation (19) indicates that the tangential velocity can be expressed as a sum of free and forced vortices. The constants C and ω in (19) depend on Ω. These constants can be estimated from the measured tangential velocity in the annular region ($0.5 < r/r_0 < 0.9$) using a least-squares method.

Figure 18 shows the variation of the constants C and ω with Ω, obtained from the

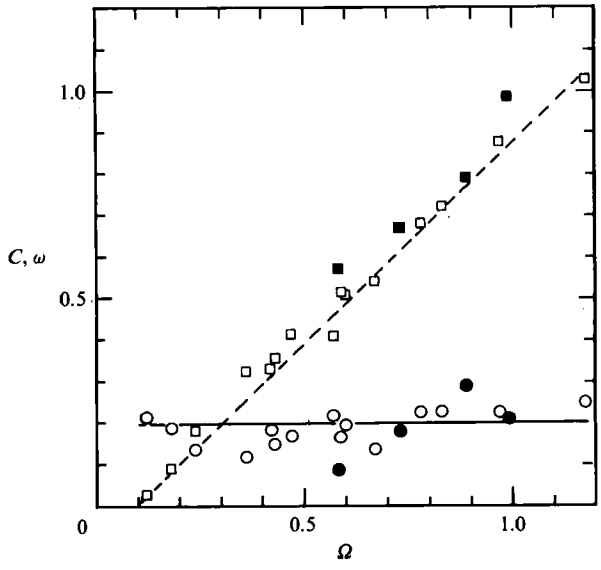

FIGURE 18. Variation of constants C and ω in equation (19) with Ω. Present: □, C; ○, ω. Seno & Nagata (1971): ■, C; ●, ω.

present data sets and Seno & Nagata's (1971) experiments. It is interesting to note the nearly constant strength of the forced vortex component in the range $0.1 < \Omega$, whereas the intensity of the free vortex decays linearly with Ω. This means that when $\Omega > 0.1$ the decay of tangential velocity is associated with the decay of free vortex motion only. The free-vortex component becomes zero when $\Omega = 0.1$. It is only after $\Omega < 0.1$ that the forced-vortex motion begins to decay.

5.3. *Core region*

In the range $0 < r/r_0 < 0.4$–0.5, the tangential velocity has a forced-vortex-type distribution with a high angular velocity. If the outer edge of the core region is defined as the maximum tangential velocity point, then it moves inside the pipe as Ω decreases.

According to the Rayleigh criterion $(\mathrm{d}/\mathrm{d}r)(rW)^2 > 0$ for stability in relation to small perturbations, the velocity profile of this type has a strong stabilizing effect on the turbulence and the small-scale turbulent motion should die out rapidly. This situation is confirmed in the next section. Thus, in the core region large-length- and timescale motions prevail. In this region it is expected that the large-scale motion could persist for a long distance downstream and indicates some history effect on the flow.

Figure 19(*a*, *b*) compares the velocity distributions U and W which have nearly the same local swirl intensity but different upstream conditions, i.e. the flows were generated by different swirlers and have different inlet swirl intensities and axial lengths. For example, Weske & Sturov (1974) adopted a special swirler that generated pure forced vortex motion by rotating a grid. The central part of the velocity differs significantly for each case, whereas the profiles in the annular region are similar. These results indicate the long history effects in the core region.

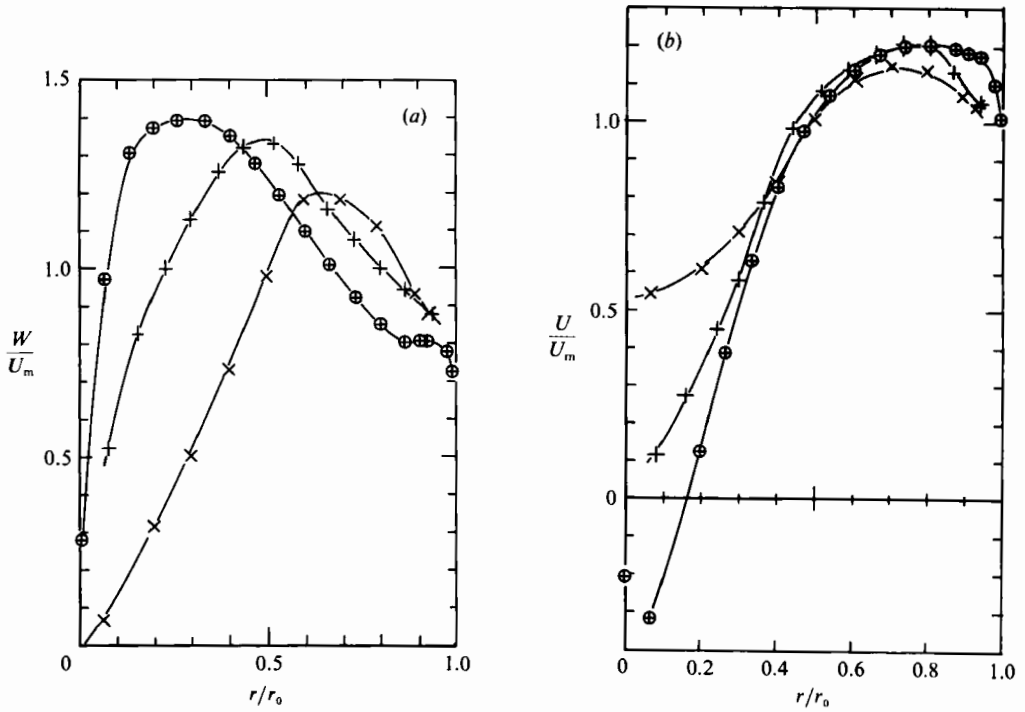

FIGURE 19. Velocity distributions (*a*) W and (*b*) U having nearly the same swirl intensity but different upstream conditions. ⊕, Present, Run 1, TS 8; +, Seno & Nagata (1972), $\Omega = 0.73$, $Re = 19 \times 10^4$, $x/d = 19$; ×, Weske & Sturov (1974), $\Omega = 0.68$, $Re = 3 \times 10^4$, $x/d = 20$.

6. Turbulence measurements

Figure 20 (*a–f*) shows the successive changes of the normal stresses $\overline{u_i^2}$ and their production $P(\overline{u_i^2})$ from the upstream to the downstream direction measured by the ×-wire system. In the figure the data of Weske & Sturov (1974) for swirling flow and Laufer (1952) for fully developed pipe flow, $Re = 5 \times 10^4$, are also included for comparison. Weske & Sturov's curves are not very accurate, because reproduction from the original small-sized drawings causes considerable uncertainty. Owing to the excess turbulent production of $\overline{v^2}$, $\overline{w^2}$ by the swirling velocity and $\overline{u^2}$ by the large axial velocity gradient in the core region (see table 4) every component has a larger energy than Laufer's data. Among the three components, $\overline{v^2}$ shows the most significant increase, becoming about three times larger than the parallel flow data when $\Omega = 0.9$. This might be a factor in an important practical application where a high heat transfer rate is observed in a swirling flow (Smithberg & Landis 1964). As a result of the high $\overline{v^2}$, the region $\overline{v^2} - \overline{u^2} > 0$ appears in the annular region where the production terms of these terms are also $P(v^2) > P(u^2)$. While the turbulent intensity in the annular region reduces gradually as swirl decays, it increases in the core region.

Table 5 shows the values of $\overline{u^2}/k$ and $(\overline{v^2} + \overline{w^2})/k$ at positions of vanishing mean strain. Predicted values from the LRR and Gibson & Younis (1986) (GY) models, equations (16) and (17), are compared in the table. For the empirical constants in the model, C_1 and C_2, the LRR model adopted $C_1 = 1.5$ and $C_2 = 0.6$ ($C_2' = 0.4$ for an elaborate version) to fit the data from homogeneous shear flow. The GY model adopted $C_1 = 3$ and $C_2 = 0.3$ to include the effect of streamline curvature in the

model. Both models predict $(\overline{v^2}+\overline{w^2})/k$ quite well. However, the predicted values of $\overline{u^2}/k$ are 20% lower than the experimental ones. This inconsistency is caused by the low C_2 which is a constant of the rapid term. In the absence of mean strain, $\partial U/\partial r = 0$, the rapid part $\frac{1}{3}C_2 P'$ is the main source of $\overline{u^2}$ energy and a large C_2 is required to fit the experimental results. The elaborate version of the LRR model predicts $\overline{u^2}/k$ better. In this version a larger constant, α, of the rapid term is adopted.

Figure 21 (*a–c*) show the distributions of the Reynolds shear stress $\overline{u_i u_j}$ across the section. $\overline{uv}$ changes sign at some radial position, but, unlike the result from the conventional eddy viscosity model, the position of the sign change does not coincide with the point $\partial U/\partial r = 0$ indicated by arrows in figure 21 (*a*). As a check, the shear stress $\overline{uv}$ is also estimated from the momentum balance equation,

$$\frac{1}{\rho}\tau_{xr} = -\overline{uv} + \nu\frac{\partial U}{\partial r} = UV + \frac{1}{r}\int_0^r r\frac{\partial}{\partial x}(U^2)\,\mathrm{d}r + \frac{1}{r}\int_0^r r\frac{\partial}{\partial x}\left(\frac{P}{\rho}\right)\mathrm{d}r.$$

Each term except the viscous stress is shown in figure 22 (*a*). The consistency of the shear stress and the Reynolds stress is fairly good. The momentum flux change along x is almost balanced by the momentum transport by the radial velocity and the shear stress is nearly equal to the integral of the pressure gradient across the section.

The distributions of $\overline{vw}$ are shown in figure 21 (*b*). The variation of various terms in the angular momentum balance equation (2) are shown in figure 22 (*b*). In the annular region, convection terms of angular momentum in the axial and radial directions make nearly the same contributions to the shear stress.

The values of $\overline{uw}$ should be predominantly positive so that they can transfer angular momentum to the downstream section. The present results show that in the region $0.2 < r/r_0 < 0.6$, $\overline{uw}$ has a large positive value, while in the range $0.6 < r/r_0 < 0.9$, where the tangential velocity is of the free-vortex type, small values of $\overline{uw}$ prevail. Gibson & Younis (1986) discussed the important role of $\overline{uw}$ in swirling jets as a production term in the transport equation of $\overline{uv}$. They indicated that a positive $\overline{uw}$ was crucially important for obtaining an appropriate $\overline{uv}$ distribution in predicting the flow. Figure 23 shows two production terms of $\overline{uv}$ (i.e. $\overline{v^2}\,\partial U/\partial r$ and $\overline{uw}W/r$) in the present case. Because of the large $\overline{v^2}$ and $\partial U/\partial r$, the former is significantly larger than the latter. This means that $\overline{uw}$ has a minor effect on $\overline{uv}$ production, unlike the case for the swirling jet.

Using the measured $\overline{u_i u_j}$ the eddy viscosities ν_{txr}, $\nu_{t\phi r}$ and $\nu_{t\phi x}$ are calculated from the following relations:

$$\nu_{txr} = -\frac{\overline{uv}}{\partial U/\partial r}, \quad \nu_{t\phi r} = -\frac{\overline{vw}}{r\,\partial/\partial r(w/r)}, \quad \nu_{t\phi x} = -\frac{\overline{uw}}{\partial w/\partial x}.$$

Figure 24 (*a–c*) shows the eddy viscosity distributions across the section. The data scatter widely, but show some relation with r. The large anisotropy among the three components can be seen, and this result is consistent with Lilley & Chigier's (1971) report on the anisotropic nature of turbulent viscosity in swirling flow. Very close to the wall the anisotropy becomes weak. Kobayashi & Yoda (1987) adopted $k-\epsilon$ model to simulate swirling flow and concluded that the standard model did not predict the velocity distribution well. However, they could obtain a satisfactory result when an anisotropy factor a_{ij} was introduced in the relation $\nu_{tij} = a_{ij} C k^{\frac{1}{2}}/\epsilon$.

Figure 25 indicates the ratio of shear stress to twice the turbulent kinetic energy $\overline{q^2}$, $a_i = (\overline{uv}^2 + \overline{vw}^2)^{\frac{1}{2}}/\overline{q^2}$, for various swirl intensities. For a two-dimensional flow Bradshaw, Ferris & Atwell (1967) obtained good numerical results by putting $a_i = 0.15$. Recently Müller (1982*a*) reported that even in a skewed boundary layer the

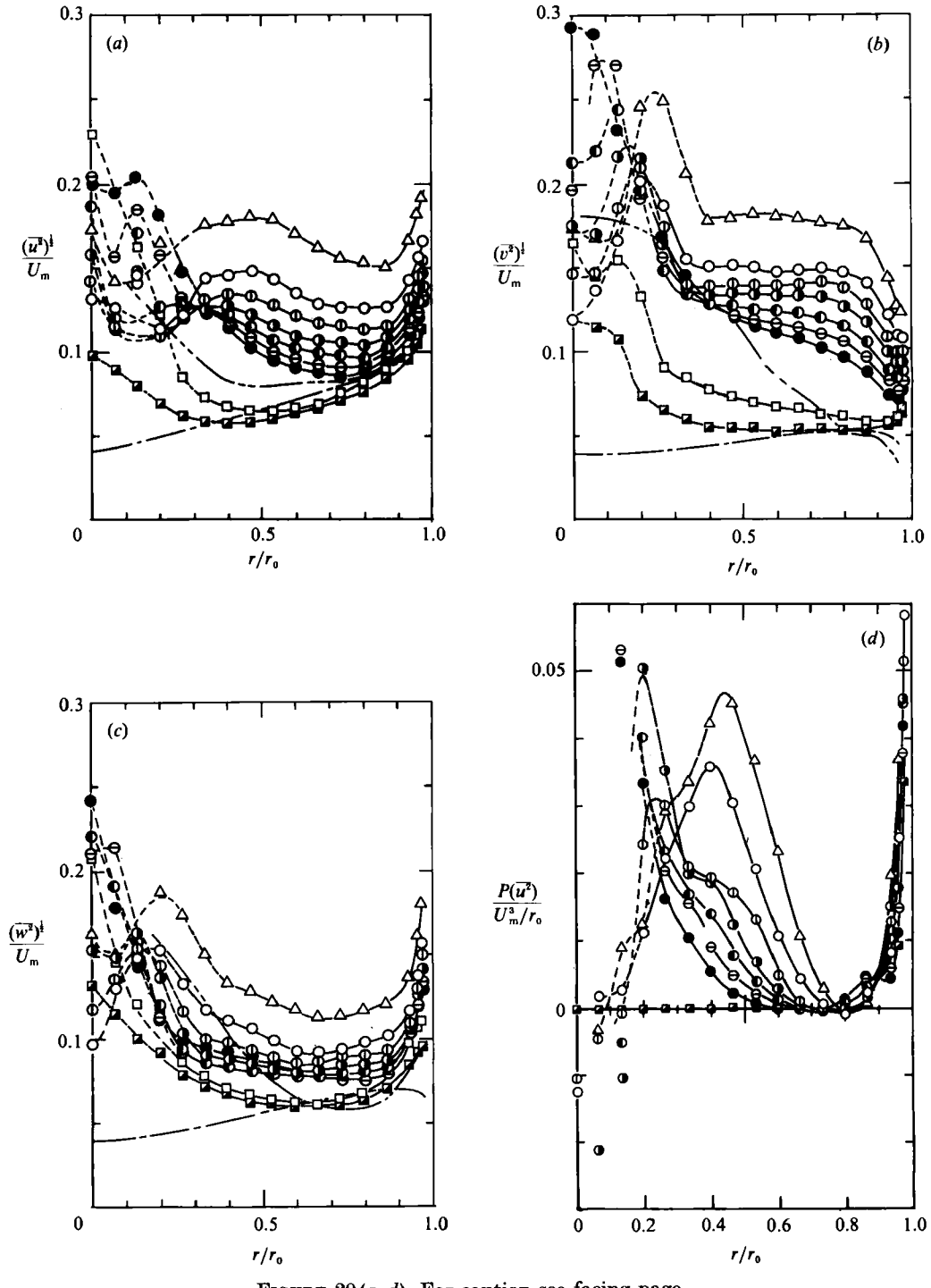

FIGURE 20 (*a–d*). For caption see facing page.

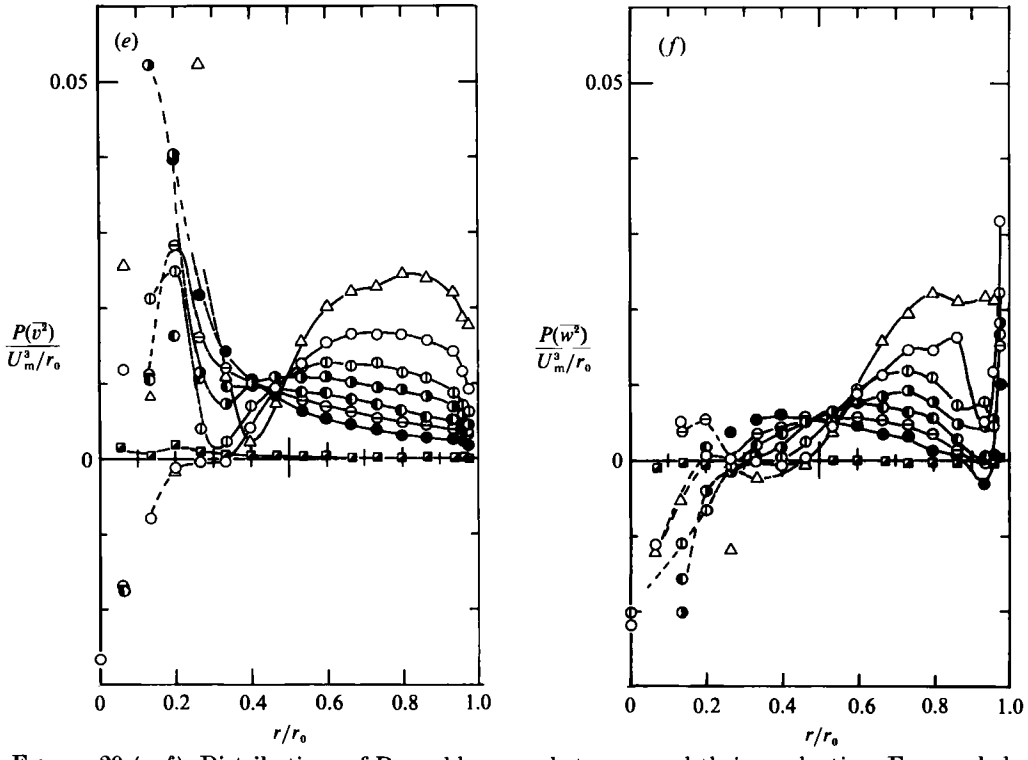

FIGURE 20 (*a–f*). Distributions of Reynolds normal stresses and their production. For symbols, see figure 11. —·—, Laufer (1952); —··—, Weske & Sturov (1974).

	Swirling flow	Parallel flow
$\overline{u^2}$	$-2\overline{uv}\dfrac{\partial U}{\partial r}$	$-2\overline{uv}\dfrac{\partial U}{\partial r}$
$\overline{v^2}$	$2\overline{vw}\dfrac{W}{r}$	0
$\overline{w^2}$	$-2\overline{vw}\dfrac{\partial W}{\partial r}$	0
$\frac{1}{2}\overline{Q^2}$	$-\overline{uv}\dfrac{\partial U}{\partial r}-\overline{vw}\left(\dfrac{\partial W}{\partial r}-\dfrac{W}{r}\right)$	$-\overline{uv}\dfrac{\partial U}{\partial r}$
$\overline{uv}$	$-\overline{v^2}\dfrac{\partial U}{\partial r}+\overline{uw}\dfrac{W}{r}$	$-\overline{v^2}\dfrac{\partial U}{\partial r}$
$\overline{vw}$	$-\overline{v^2}\dfrac{\partial W}{\partial r}+\overline{w^2}\dfrac{W}{r}$	0
$\overline{uw}$	$-\overline{vw}\dfrac{\partial U}{\partial r}-\overline{uv}\dfrac{\partial W}{\partial r}$	0

TABLE 4. Production terms of turbulent kinetic energy.

		Experiment	LRR model		GY model
			Simplified	Elaborate	
$\frac{\overline{u^2}}{k}$	at $\partial U/\partial r = 0$	0.684 ~ 0.626 (Run 8, TS 1 ~ TS 10)	0.489	0.609	0.511
$\frac{\overline{v^2}+\overline{w^2}}{k}$	at $\partial W/\partial r - W/r = 0$	1.098 (Run 10, TS 7)			
		1.078 (Run 10, TS 10)	0.978		1.022

TABLE 5. Comparison of $\overline{u_i^2}/k$ predicted from Reynolds stress models and experiment.

factor a_i is constant at 0.15. For a two-dimensional curved flow, however, Gills & Johnston (1983) and Barlow & Johnston (1988) indicated that the factor a_i is not constant through the boundary layer, with a trend that depends on whether the surface is convex or concave. On the concave side, unstable flow, a_i increases over 40% above 0.15, while on the convex side it decreases to under 0.15. In swirling flow a_i is far from constant; first it increases to 0.15 at $r/r_0 = 0.9$ from zero at the wall then decreases to 0.09 in the annular region. According to the Rayleigh criterion, the tangential velocity distribution in the annular and core regions is stable as in the case of a boundary layer on a convex wall, Gills & Johnston (1983). The low value of a_i in these regions could be attributed to the centrifugal stability effect, but clear evidence for this conclusion could not be given here. In the core region ($r/r_0 < 0.4$) the value decreases further.

In the annular region of highly skewed flow, the shear and velocity-gradient angles differ from each other. According to equation (13) the relation between the two angles is dominated by the sign of the leading terms of $\partial U/\partial r$ and $(\overline{w^2}-\overline{v^2})$ in the annular region. Figure 17 shows the cross-sectional variation of θ_g and θ_s. In the annular region the curves of θ_g and θ_s cross at two points. In the figure the radial position $\overline{w^2}-\overline{v^2} = 0$ is indicated by a chain dot line which corresponds to the crossing point near the wall. Figure 26 compares the measured angle relation with the Reynolds stress model, equation (13), where the measured turbulence data are used in the model. The qualitative agreement is good.

The turbulent character is expected to be different among the core, annular and wall regions because of the centrifugal stabilizing or destabilizing effect in the swirling flow. The W-distribution here satisfies the Rayleigh criterion for stability throughout the cross-section except close to the wall but we do not have any evidence of suppression of the fluctuating motion. Eskinazi & Yeh (1956) performed a two-dimensional curved flow experiment and their data indicated that the stable region estimated from the Rayleigh criterion did not exactly coincide with the area where the turbulent kinetic energy was absorbed by the mean velocity. In addition to the stabilizing/destabilizing effect of the tangential velocity, there is another energy source of the turbulence, production of $\overline{u^2}$, in the swirling flow. This additional energy source makes an important contribution to the energy balance, making the situation more complex than two-dimensional curved flow.

In the core region, because of the relation $\mathrm{d}(rW)^2/\mathrm{d}r \gg 0$, the stabilizing effect

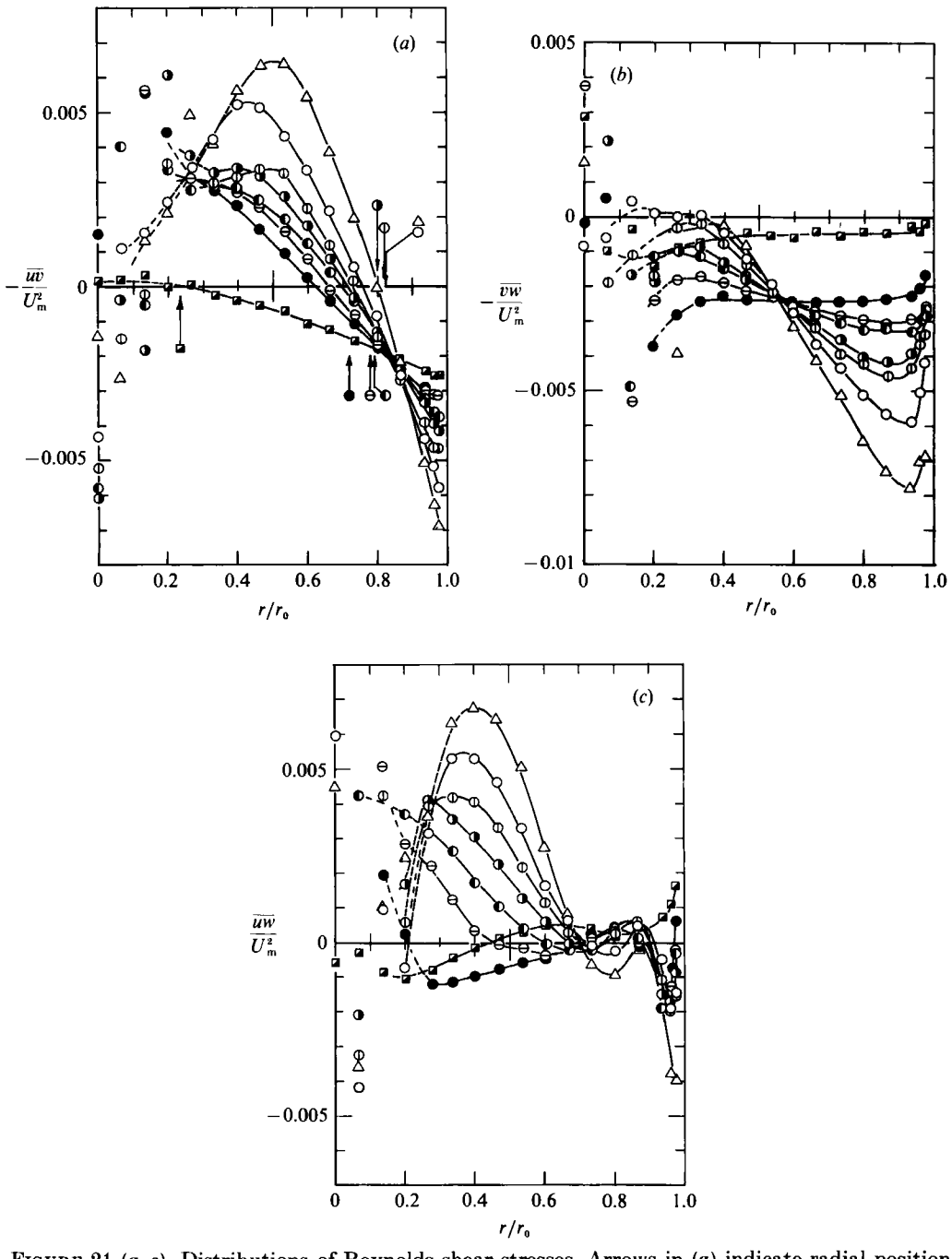

FIGURE 21 (*a–c*). Distributions of Reynolds shear stresses. Arrows in (*a*) indicate radial position of $\partial U/\partial r = 0$. For symbols, see figure 11.

would be expected to be significant. Any clear evidence of stability, however, cannot be seen because the turbulent measurements around the axis include a large uncertainty. The tendency of low $\overline{v^2}, \overline{w^2}$ found there for large Ω is the only sign of suppression of the radial and tangential fluctuating motion.

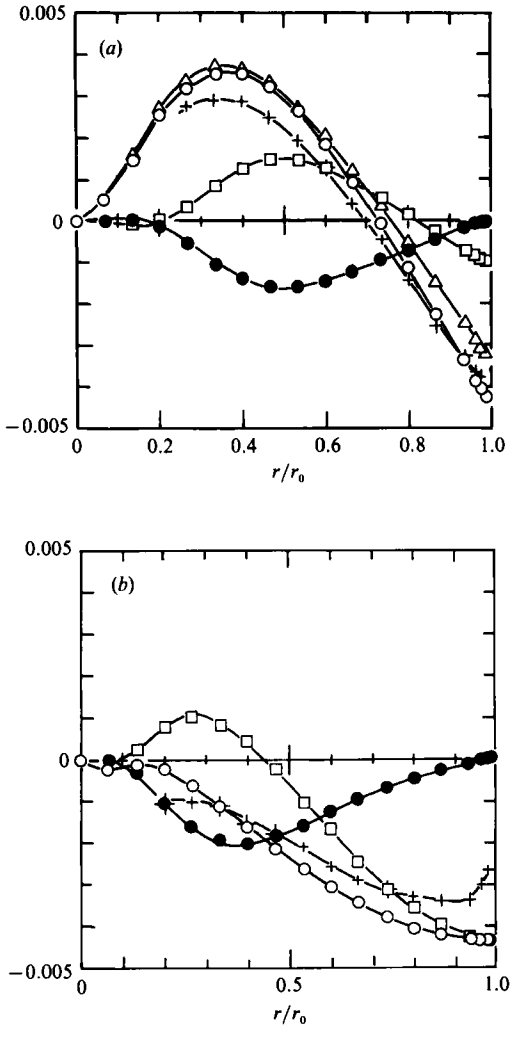

FIGURE 22. (*a*) Balance of axial momentum flux across a section. Run 8: TS 7.

$$\bigcirc, \frac{\tau_{rx}}{\rho U_m^2}; \ \bullet, \frac{UV}{U_m^2}; \ \square, \frac{1}{r}\int_0^r r\frac{\partial}{\partial x}(U^2)\,\mathrm{d}r/U_m^2; \quad \triangle, \frac{1}{r}\int_0^r r\frac{\partial}{\partial x}\left(\frac{P}{\rho}\right)\mathrm{d}r/U_m^2; \quad +, \frac{-\overline{uv}}{U_m^2}.$$

(*b*) Balance of angular momentum flux across a section. Run 8: TS 7.

$$\bigcirc, \frac{\tau_{r\phi}}{\rho U_m^2}; \quad \bullet, \frac{VW}{U_m^2}; \quad \square, \frac{1}{r^2}\int_0^r r^2\frac{\partial}{\partial x}(UW)\,\mathrm{d}r/U_m^2; \quad +, \frac{-\overline{vw}}{U_m^2}.$$

Figure 27 (*a*, *b*) shows the time trace of the velocity fluctuation and its spectrum measured in the wall, annular and core regions. In the core region very low-frequency motion prevails, while in the outer regions the fluctuation includes high-frequency motion as expected in turbulent flow. The energy spectrum of the streamwise velocity $\overline{u^2}$ also reflects this tendency. In the core region a peculiar frequency is observed and this might be the signal of an inertial wave generated by the rotating

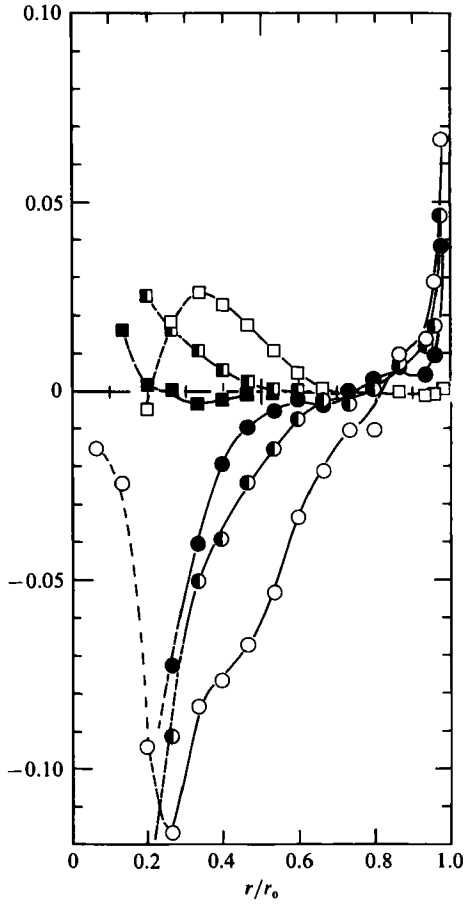

FIGURE 23. Production terms for uv, Run 8.

TS 1: ○, $-\overline{v^2}\dfrac{\partial U}{\partial r}\Big/\dfrac{U_m^3}{r_0}$; □, $\overline{uw}\dfrac{W}{r}\Big/\dfrac{U_m^3}{r_0}$.

TS7: ◐, $-\overline{v^2}\dfrac{\partial U}{\partial r}\Big/\dfrac{U_m^3}{r_0}$; ◧, $\overline{uw}\dfrac{W}{r}\Big/\dfrac{U_m^3}{r_0}$.

TS 10: ●, $-\overline{v^2}\dfrac{\partial U}{\partial r}\Big/\dfrac{U_m^3}{r_0}$; ■, $\overline{uw}\dfrac{W}{r}\Big/\dfrac{U_m^3}{r_0}$.

motion. The microscale of the turbulence λ_f, estimated on the assumption of the frozen turbulence and using the relation

$$\frac{1}{\lambda_f^2} = \frac{1}{2}\frac{1}{V_t}\frac{1}{\tilde{u}^2}\overline{\left(\frac{\partial \tilde{u}}{\partial t}\right)^2}$$

is shown in figure 28. It becomes very large in the core region when Ω is large, thus indicating the non-dissipative character of the motion here.

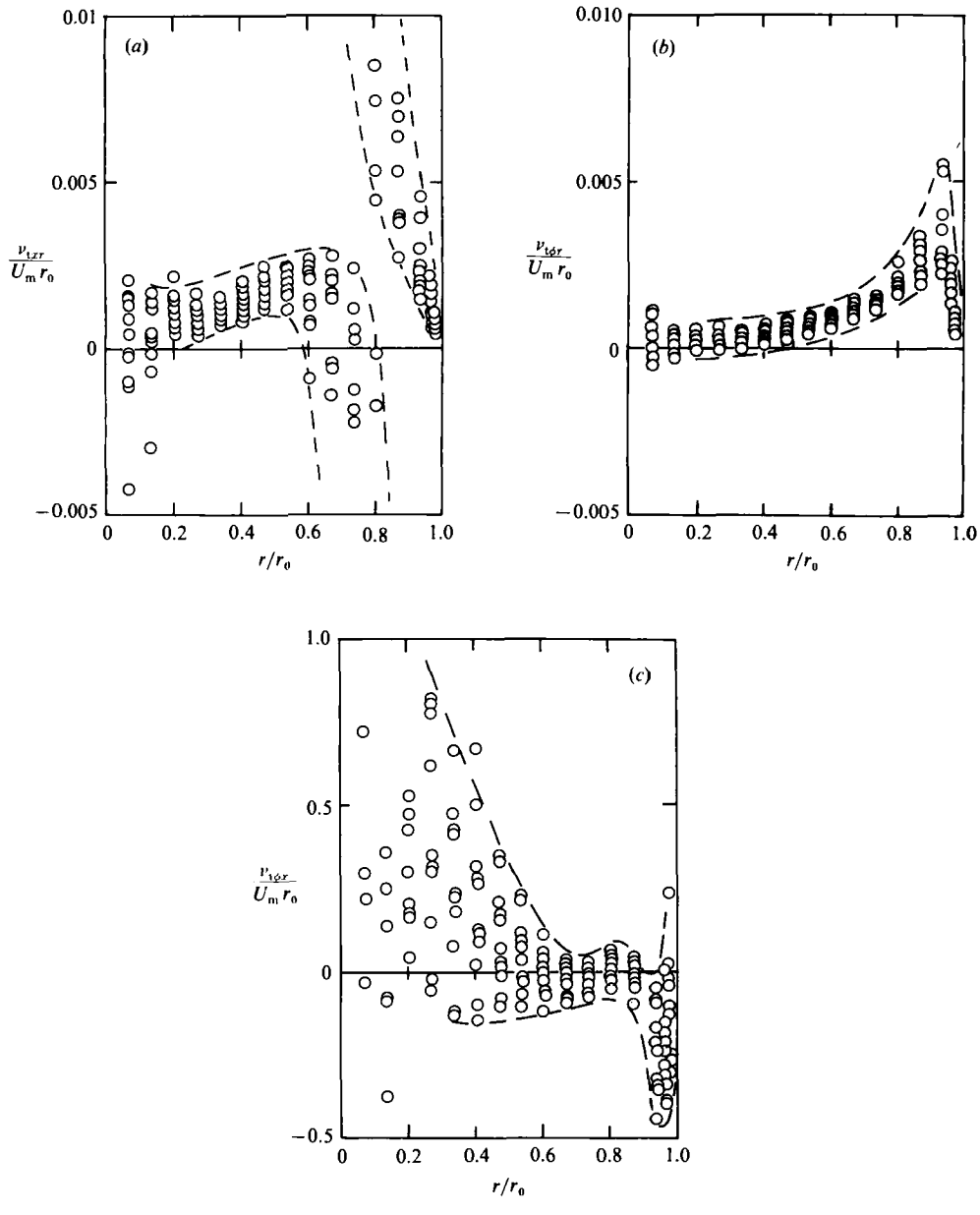

FIGURE 24. Distributions of eddy viscosities, $Re = 50000$.

7. Concluding remarks

The tangential velocity in swirling flow through a pipe has a significant influence on the flow structure. Among many factors that affect the flow, we limited consideration to the centrifugal stabilizing/destabilizing effect, flow skewness and history effects. Based on the tangential velocity distribution, the flow has three regions: wall, annular and core. In the wall region only the centrifugal destabilizing effect appears and the classical mixing-length model modified by the Monin–Oboukhov formula can predict the flow there. The coefficient β is determined to

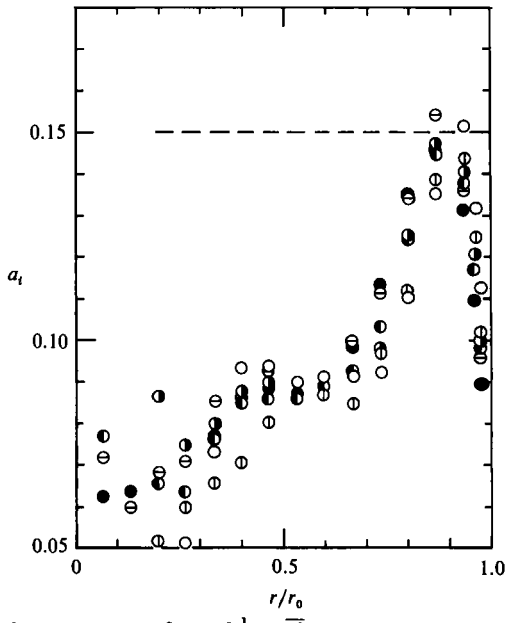

FIGURE 25. Ratio of shear stress $(\overline{uv}^2+\overline{vw}^2)^{\frac{1}{2}}$ to $\overline{q}^2$. For symbols, see figure 11. ----, $a_t = 0.15$.

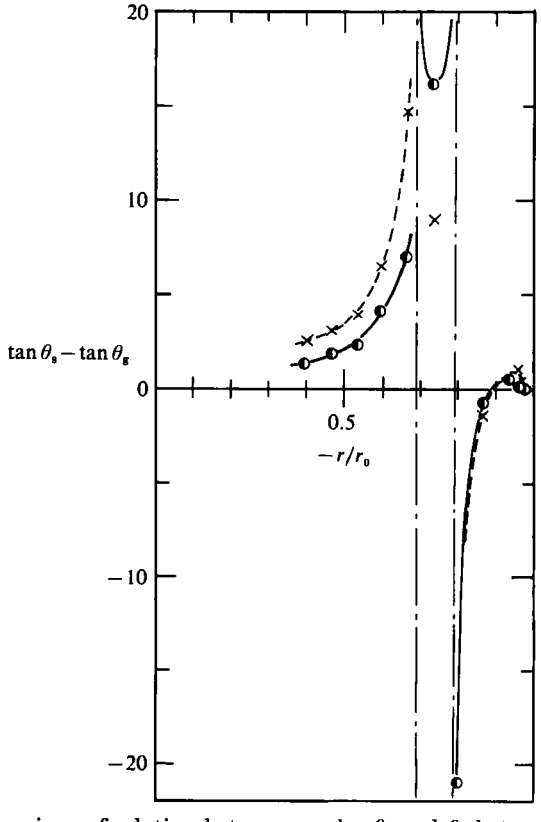

FIGURE 26. Comparison of relation between angles θ_s and θ_g between experiment and Reynolds stress model. Run 8, TS 7: ◐, experiment; ×, Reynolds stress model.

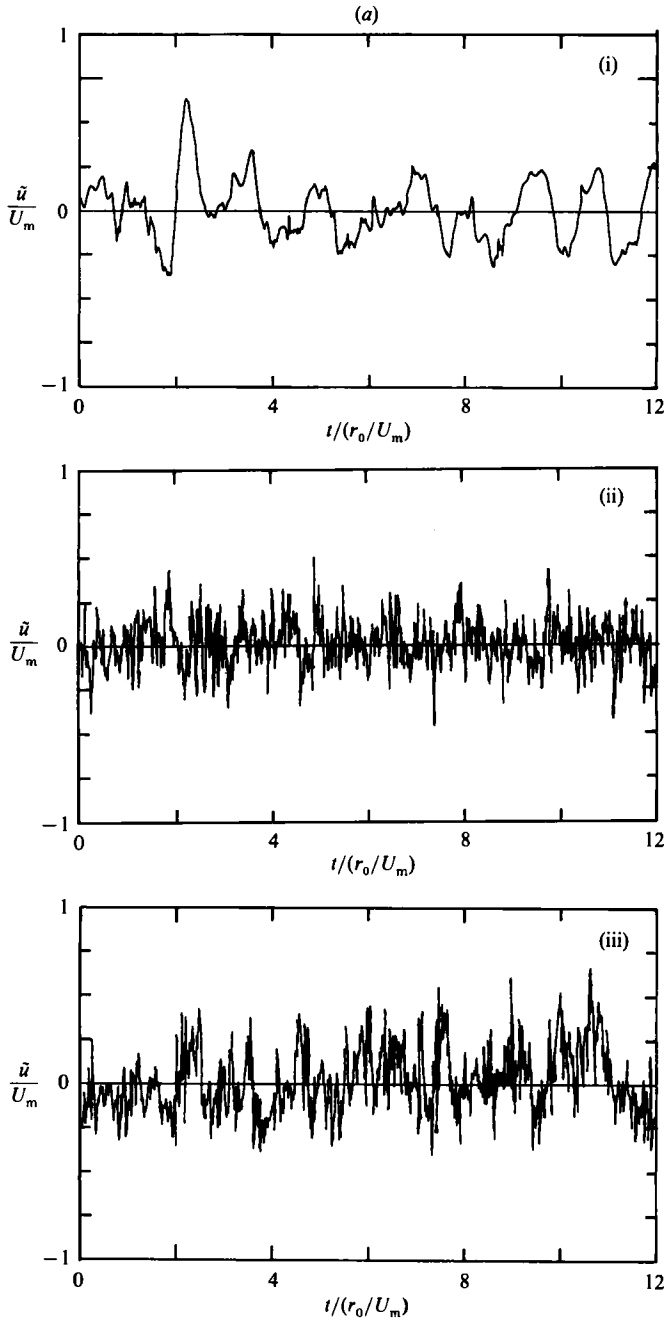

FIGURE 27(a). For caption see facing page.

be 6 to fit the experimental data that is consistent with Johnston's (1970) result. The annular region is characterized by a flow skewness and angles θ, θ_g and θ_s that are different from one another. In this region the analytical approach to predicting the flow is quite difficult. A Reynolds stress model which can handle anisotropic turbulence is a more promising means to model the flow compared to an eddy viscosity model like $k-\epsilon$. The angle relation between θ_g and θ_s based on this model

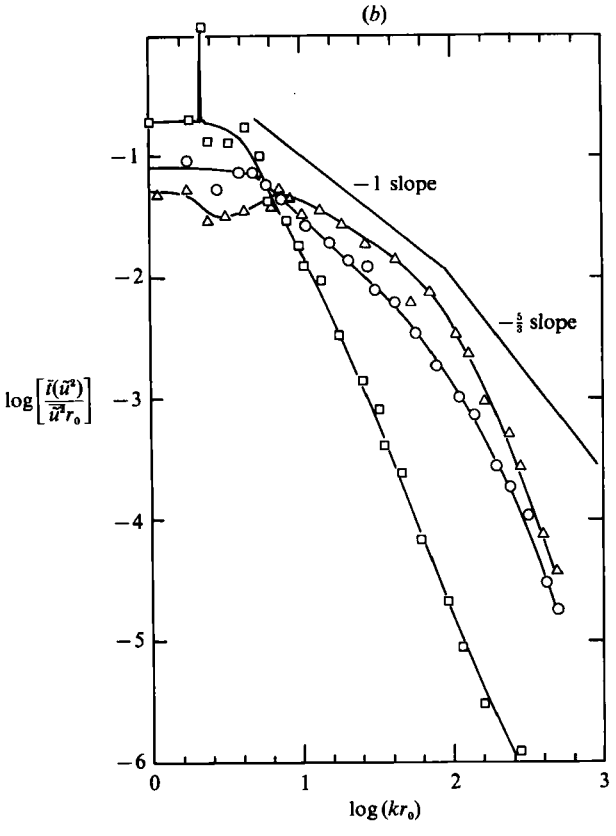

FIGURE 27. (*a*) Time records of velocity fluctuation $\tilde{u}$ at three radial positions: (i) $r/r_0 = 0.067$; (ii) $r/r_0 = 0.733$, (iii) $r/r_0 = 0.973$. Run 7, TS 3. t in abscissa indicates time. (*b*) Energy spectrum of $\tilde{u}^2$. Run 7, TS 3. k in abscissa indicates wavenumber. □, $r/r_0 = 0.067$; △, $r/r_0 = 0.733$; ○, $r/r_0 = 0.973$.

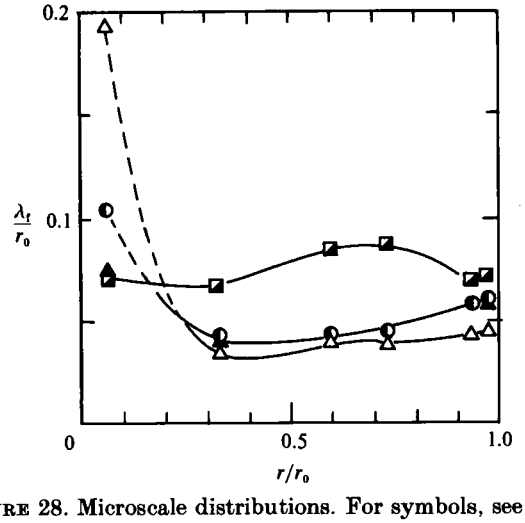

FIGURE 28. Microscale distributions. For symbols, see figure 11.

is qualitatively in agreement with the experiment. It is also noticeable that the tangential velocity could be expressed as a sum of forced and free vortex motions. In the core region, the centrifugal stabilizing effect becomes important, turbulent motion with very low-frequency prevails and the flow is non-dissipative. The inlet conditions have a large effect on the downstream flow in the core region. Thus for the core region there is a long history effect.

REFERENCES

ALLEN, J. M. 1977 Experimental study of error sources in skin-friction balance measurements. *Trans. ASME* I: *J. Fluids Engng* **99**, 197.

BACKSHALL, R. G. & LANDIS, F. 1969 The boundary-layer velocity distribution in turbulent swirling pipe flow. *Trans. ASME* D: *J. Basic Engng* **91**, 728.

BAKER, D. W. 1967 Decay of swirling, turbulent flow of incompressible fluids in long pipes. Dissertation, University of Maryland.

BARLOW, R. S. & JOHNSTON, J. P. 1988 Structure of a turbulent boundary layer on a concave surface. *J. Fluid Mech.* **199**, 137.

BISSONETTE, L. R. & MELLOR, G. L. 1974 Experiments on the behaviour of an axisymmetric turbulent boundary layer with sudden circumferential strain. *J. Fluid Mech.* **63**, 369.

BRADSHAW, P. 1969 The analogy between streamline curvature and buoyancy in turbulent shear flow. *J. Fluid Mech.* **36**, 177.

BRADSHAW, P. 1971 Calculation of three-dimensional turbulent boundary layers. *J. Fluid Mech.* **46**, 417.

BRADSHAW, P., FERRIS, D. H. & ATWELL, N. P. 1967 Calculation of boundary-layer development using the turbulent energy equation. *J. Fluid Mech.* **28**, 593.

ESKINAZI, S. & YEH, H. 1956 An investigation on fully developed turbulent flows in a curved channel. *J. Aero Sci.* **23**, 23.

GIBSON, M. M. & YOUNIS, B. A. 1986 Calculation of swirling flow jets with a Reynolds stress closure. *Phys. Fluids* **29**, 38.

GILLS, J. C. & JOHNSTON, L. P. 1983 Turbulent boundary-layer flow and structure on a convex wall and its redevelopment on a flat wall. *J. Fluid Mech.* **135**, 123.

HIRAI, S., TAKAGI, T. & MATSUMOTO, M. 1988 Prediction of the laminarization phenomena in an axially rotating pipe flow. *Trans. ASME* I: *J. Fluids Engng* **110**, 424.

HIRAI, S., TAKAGI, T., TANAKA, K. & KIDA, K. 1987 Effect of swirl on the turbulent transport of momentum in a concentric annular with a rotating cylinder. *Trans. JSME* B **53**, 432.

JOHNSTON, J. P. 1970 Measurements in a three-dimensional turbulent boundary layer induced by a swept, forward-facing step. *J. Fluid Mech.* **42**, 823.

JOHNSTON, J. P., HALLEEN, R. M. & LEZIUS, D. K. 1972 Effects of spanwise rotation on the structure of two-dimensional fully developed turbulent channel flow. *J. Fluid Mech.* **56**, 533.

KITO, O. 1984 Axi-asymmetric character of turbulent swirling flow in a straight circular pipe. *Bull. JSME* **27**, 683.

KITO, O. & KATO, T. 1984 Near wall velocity distribution of turbulent swirling flow in circular pipe. *Bull. JSME* **27**, 1659.

KLEIN, S. J., CANTWELL, B. J. & LILLEY, G. M. 1980–81 *AFOSR–HTTM–Stanford Conference on Complex Turbulent Flows.*

KOBAYASHI, T. & YODA, M. 1987 Modified $k-\epsilon$ model for turbulent swirling flow in a straight pipe. *JSME Intl J.* **30**, 66.

LAUFER, J. 1952 The structure of turbulence in fully developed pipe flow. *NACA Tech. Rep.* 1174.

LAUNDER, B. E., REECE, G. J. & RODI, W. 1975 Progress in the development of a Reynolds-stress turbulence closure. *J. Fluid Mech.* **68**, 537.

LILLEY, D. G. & CHIGIER, N. A. 1971 Nonisotropic turbulent stress distribution in swirling flows from mean value distributions. *Intl J. Heat Mass Transfer* **14**, 573.

MÜLLER, U. R. 1982*a* Measurement of the Reynolds stresses and the mean-flow fields in a three-dimensional pressure driven boundary layer. *J. Fluid Mech.* **119**, 121.

MÜLLER, U. R. 1982*b* On the accuracy of turbulence measurements with inclined hot wires. *J. Fluid Mech.* **119**, 155.

PADMANABHAN, M. & JANEK, C. R. 1980 Swirling flow and its effect on wall pressure drop within pipes. In *Vortex Flows: ASME Meeting 1980* (ed. W. L. Swift, P. S. Barna & C. Dalton), p. 65. ASME.

PERRY, A. E. & JOUBERT, P. N. 1965 A three-dimensional turbulent boundary layer. *J. Fluid Mech.* **22**, 285.

REYNOLDS, A. 1961 On the dynamics of turbulent vortical flow. *Z. Angew. Math. Phys.* **12**, 149.

SENO, Y. & NAGATA, T. 1971 Swirling flow through a long straight pipe (4th report). *Preprint of Annual meeting of JSME No.* 710-3, p. 149. (In Japanese.)

SENO, Y. & NAGATA, T. 1972 Swirl flow in long pipes with different roughness. *Bull. JSME* **15**, 1514.

SMITHBERG, E. & LANDIS, F. 1964 Friction and forced convection heat-transfer characteristics in tubes with twisted tape swirl generators. *Trans. ASME* C: *J. Heat Transfer* **86**, 39.

SO, R. M. 1975 A turbulent velocity scale for curved shear flows. *J. Fluid Mech.* **70**, 37.

TOWNSEND, A. A. 1976 *The Structure of Turbulent Shear Flow*, 2nd edn, p. 398. Cambridge University Press.

VAN DEN BERG, B. 1982 Some notes on three-dimensional turbulent boundary layer data and turbuence modelling. *IUTAM Symp. on Three-dimensional turbulent boundary layers, Berlin* (ed. H. Fernholz & E. Krause), p. 1. Springer.

WESKE, D. R. & SUTROV, G. YE. 1974 Experimental study of turbulent swirled flows in a cylindrical tube. *Fluid Mech. Sov. Res.* **3**, 77.

YAJNIK, K. S. & SUBBAIAH, M. V. 1973 Experiments on swirling turbulent flows. Pt. 1. Similarity in swirling flows. *J. Fluid Mech.* **60**, 665.